CHALMERS

Cold spray Cr-coated Optimized ZIRLO claddings: an option for accident tolerant fuels

Andrea Fazi

Cold spray Cr-coated Optimized ZIRLO claddings: an option for accident tolerant fuels

Andrea Fazi

Cover illustration

Left: APT reconstruction of the intermixed bonding region found at the Cr/Zr interface of an as-fabricated CS-Cr coated Optimized ZIRLO[TM] cladding. Centre: BF-TEM images of the Cr/Zr interface of an as-fabricated (top) and autoclave exposed (bottom) CS-Cr coated Optimized ZIRLO[TM] cladding. Right: APT reconstruction of the Zr-Cr-Fe phase found in the substrate adjacent to the Cr/Zr interface of an exposed CS-Cr coated Optimized ZIRLO[TM] cladding.

Cold spray Cr-coated Optimized ZIRLO claddings: an option for accident tolerant fuels

Andrea Fazi
Department of Physics
Chalmers University of Technology

ABSTRACT

Accident tolerant fuel development has started with the aim of providing nuclear fuels able to endure severe accident conditions. Research in this field has also sparked a wave of material renewal in the nuclear industry that had being delayed for the last few decades. Climate change is an ever-growing public concern, and policies about greenhouse gas emissions are becoming more stringent both at the national and international level. Nuclear energy produces very low carbon emissions and the successful development of new accident tolerant materials might play a role in making this technology a viable solution to this global issue. Cr-coated zirconium claddings are one of the most promising candidates as near-term response to the need for accident tolerant materials. These coatings can be produced via a range of different technologies, but the two main designs being currently developed are obtained with physical vapour deposition or cold spray (CS) deposition. In cold spray, high pressure gas is fed through a nozzle together with Cr powder. The Cr particles are accelerated up to 1200 m/s and directed to the substrate, in this case cladding tubes made of Optimized ZIRLO™ alloy. The resulting Cr-coated zirconium cladding is the subject of this work.

As-fabricated samples and autoclave tested material are characterized with atom probe tomography and a range of electron microscopy techniques. The scope of the investigation is to evaluate the performances of Cr-coated claddings under operating conditions. Additionally, the nature of the adhesion in cold spray coating and the effects of this deposition method on the substrate are explored. A 10-20 nm thick intermixed bonding region was observed at the Cr/Zr interface of the as-fabricated cladding. This region is deemed to play an important role in the strong adhesion of CS coatings. When exposed to operating conditions, $ZrCr_2$-Laves phase was found to nucleate in the intermixed bonding region. CS deposition involves severe plastic deformation of both coating and substrate. As a result, a 1-2 µm thick nanocrystalline layer can be found in the substrate adjacent to the Cr/Zr interface. After autoclave exposure, a Zr-Cr-Fe phase was discovered precipitating in this nanocrystalline layer at the Zr grain boundaries.

PREFACE

The work presented in this thesis was performed at the Division of Microstructure Physics, Department of Physics, Chalmers University of Technology, during the period 2018-2021, under the supervision of Associate Professor Mattias Thuvander.

LIST OF APPENDED PAPERS

i. *Characterization of as-deposited cold sprayed Cr-coating on Optimized ZIRLO™ claddings*
A. Fazi, H. Aboulfadl, A.H.S. Iyer, M. Sattari, K.M. Stiller, P. Lokhande, M. Thuvander, H.O. Andrén
Journal of Nuclear Materials 549, p.152892 (2021)

ii. *Cold sprayed Cr-coating on Optimized ZIRLO™ claddings: the Cr/Zr interface and its microstructural and chemical evolution after autoclave corrosion testing.*
A. Fazi, K.M. Stiller, H.O. Andrén , M. Thuvander.
In manuscript

CONTRIBUTIONS

My contributions to the papers listed above:

i. Performed specimen preparation by FIB/SEM, most of the APT measurements, data analysis and interpretation, EBSD mapping, TKD mapping, TEM imaging, and wrote the paper with input from the co-authors. Nano-hardness measurements and HR-TEM were not performed by the first author.

ii. Performed specimen preparation by FIB/SEM, APT measurements, data analysis and interpretation, SEM imaging, EDS analysis, EBSD mapping, TEM imaging, and wrote the paper with input from the co-authors.

LIST OF ACRONYMS

ADF   Annular dark field

AE   Auger electrons

APT   Atom probe tomography

ATF   Accident tolerant fuel

BF-TEM   Bright field TEM

BIB   Broad ion beam

BSE   Backscattered electrons

BWR   Boiling water reactor

CS   Cold spray

EBSD   Electron backscattered diffraction

EELS   Electron energy loss spectroscopy

EFTEM   Energy filtered TEM

ESEM   Environmental SEM

FIB   Focussed ion beam

GIS   Gas injection system

HAADF   High angle annular dark field

HWR   Heavy water reactor

IBR   Intermixed bonding region

LOCA   Loss of coolant accident

LWR   Light water reactor

OPZ   Optimized ZIRLO

PWR   Pressurized water reactor

SAD   Selected area diffraction

SE   Secondary electrons

SEM   Scanning electron microscopy

SPP   Secondary phase particle

STEM   Scanning TEM

TEM   Transmission electron microscopy

TKD   Transmission Kikuchi diffraction

TABLE OF CONTENTS

x

INTRODUCTION

Nuclear energy represents around 5% of the total world energy production (2657 TWh in 2019) and it is characterized by extremely low carbon emissions. The effects of greenhouse gases are becoming a global concern, national and international regulatory bodies are issuing policies with the objective of driving change in the way electricity is produced, and nuclear power is seen as one of the technologies that can help in this transition. New reactor concepts, such as small modular reactors and fast neutron reactors, are being developed to improve two of the most problematic aspects of nuclear energy: the extremely high upfront costs of building new power plants and nuclear waste production [1]. However, the deployment of these new designs in commercial reactors will require several more years. Of the 442 nuclear power plants currently operable or in commercial operation, 365 are light water reactors (LWRs). Consequently, LWRs produce approximately 90% of the total nuclear energy output. Beyond the already existing plants, about 50 additional nuclear power plants are currently being constructed around the world, particularly in China, India, Russia and the United Arab Emirates; of these, the large majority are LWRs [2,3].

Since the Fukushima Daiichi accident in 2011, the concept of accident tolerant fuels (ATFs) has emerged in the nuclear industry with the intent of developing safer and more functional nuclear fuel designs for LWRs. The idea behind ATF is to develop nuclear fuels able to better survive severe accident conditions while modernizing the nuclear industry; allowing this technology to better serve society in the important decades of green revolution that are to come. Amongst the many areas of research in this field, Cr-coatings have attracted attention for their exceptional performance both under normal operating conditions and under severe accident conditions. This family of coatings is bringing forward the development of the coated zirconium cladding as one of the possible solutions for ATFs. A lot of work is currently being done worldwide to bring these materials from the development stage towards their commercial use. The nuclear industry is one of the most heavily regulated in the energy production sector, and new materials have to go through extensive testing and licencing before their use is allowed in a commercial reactor. For this reason, the detailed characterization of such materials is of crucial importance in creating a clear understanding of their behaviour in both operating and accident conditions. Cold spray (CS) is a novel technology used for additive manufacturing and coating deposition, and it is one of the methods currently being used to deposit Cr-coatings for ATF applications. CS does not require vacuum or heating of the substrate, and it can be used to quickly grow dense coatings in a large range of thicknesses, making it a well-suited technique for large scale production. The basics about LWRs and an introduction to ATFs are presented in Chapter 2. More details about CS technology are reported in Chapter 3.

In this work, zirconium fuel rods coated with metallic Cr using CS deposition are extensively studied through the employment of numerous characterisation techniques. This material is one of the candidate ATF coating designs for pressurised water reactors (PWRs). Samples both

as-fabricated and exposed to simulated operating conditions are examined. The main intent is to collect data relevant for the performance assessment of the coating/substrate system. The possibility of studying the same material before and after exposure was crucial in determining trends in the microstructural and chemical evolution of coating and substrate. The materials and characterization techniques used are reported and explained in Chapter 4. A summary of the main results is shown in Chapter 5.

1.1 AIM OF THE STUDY

The two main aspects driving this research were the identification of advantages and disadvantage of CS as deposition technology of choice for ATF applications, and the study of the Cr-coated cladding behaviour in simulated operating conditions. Because the deposition method can affect the properties of the obtained coating and consequently the ATF performance, there is significant interplay between these two aspects and they cannot be considered separately. Cold spray Cr-coatings have demonstrated exceptional adhesion properties. No spallation of the coating has been reported, even when tested under extreme thermal or mechanical conditions [4]. The main objective of the coating is to improve high temperature steam corrosion resistance of the cladding and the ability to survive a wide range of conditions without being damaged and losing its effectiveness is instrumental. Strong adhesion is one advantage of CS, and exploring this aspect was deemed important for understanding the origin of this phenomenon. In addition, the microstructure of the zirconium alloys is finely tuned to reliably provide specific properties to the cladding tubes and the application of a corrosion resistant coating should not affect the performance of the substrate. Hence, the effects of the deposition method on the substrate need to be taken into account. These effects must be identified, and their relevance on the overall behaviour of the cladding has to be estimated. While in operation, most of the evaluation of the rod conditions is performed combining models with the reading of certain external parameters. Building the models needed for such a scope requires profound comprehension of all the phenomena that can occur on the coated cladding rod once it is in operation, for example, microstructural or chemical changes, and the rates at which these changes happen. Although the primary reason behind the potential adoption of Cr-coating in nuclear fuels is to act as protection in case of a severe accident, this coating needs to perform at least as good as traditional materials in normal operation, especially in regard of oxidation. Determining rates and mechanisms by which the coating oxidises and is eventually consumed is another very important aspect needed to calculate fuel life.

Overall, this work can be divided into the following main research questions:

- *What is the origin of the strong adhesion of cold spray coatings?*

- *Does cold spray deposition produce significant modifications of the zirconium substrate?*

- *Does the coating/substrate system undergo microstructural and chemical transformations when exposed to normal operating conditions?*

- *To what degree is the Cr-coating enhancing the corrosion resistance of the zirconium cladding?*

CHAPTER 2

ACCIDENT TOLERANT MATERIALS FOR LIGHT WATER REACTOR FUELS

2.1 LIGHT WATER NUCLEAR REACTORS

2.1.1 BASIC CONCEPTS

In a nuclear reactor, the heat produced by a controlled fission reaction is transmitted to a coolant, the heat is subsequently transferred to water so to produce steam, the steam is used to power a steam turbine and produce electricity. Some of the main elements of a nuclear reactor are: fuel, moderator, coolant, control rods, steam generator and containment. Uranium oxide (UO_2 or urania) is the basic fuel. Small pellets of UO_2 are arranged inside cladding tubes to form fuel rods. Many fuel rods assembled together form a fuel assembly. The coolant and the neutron moderator used in the core can vary, but it is most often water. Water in a nuclear reactor, not only acts as a coolant transporting heat away from the core, but it acts also as moderator. The role of the moderator is to slow down fast neutrons produced during fission and to reduce their mean free path so to cause more fission. In some reactors, deuterium-enriched water (heavy water) is used as coolant and moderator. These reactors are called heavy water reactors (HWRs). The reactors where normal water is used as coolant and moderator are instead referred to as light water reactors (LWRs). Inside the core of a LWR, fission is initiated and sustained by a neutron flux. To control the neutron flux, control rods are inserted into the core. Additionally, neutron adsorbers can be added to the cooling water. The coolant coming from the core is then directed to a steam generator where the heat from the fission reaction is used to produce high pressure steam fundamental for operating the steam turbine that ultimately generates power.

LWRs can be further divided into pressurized water reactors (PWRs) and boiling water reactors (BWRs). PWR is the most common type of reactor (302 out of 442 of the total operable nuclear reactors in the world are PWRs). In this design water acts both as moderator and coolant and it is circulated in two separate loops. The primary cooling circuit water flows through the core at high pressure and temperature (around 150 bar and 325°C), while the secondary circuit is kept at lower pressures and used to generate steam. In BWRs, instead, a single water circuit is used. Water is let flow in the core at 75 bar and 285°C, these conditions are designed to have about 12-15% of the water in the top part of the core as steam. The same steam is used to drive the steam turbine. A schematic representation of PWR and BWR designs is presented in Figure 2-1.
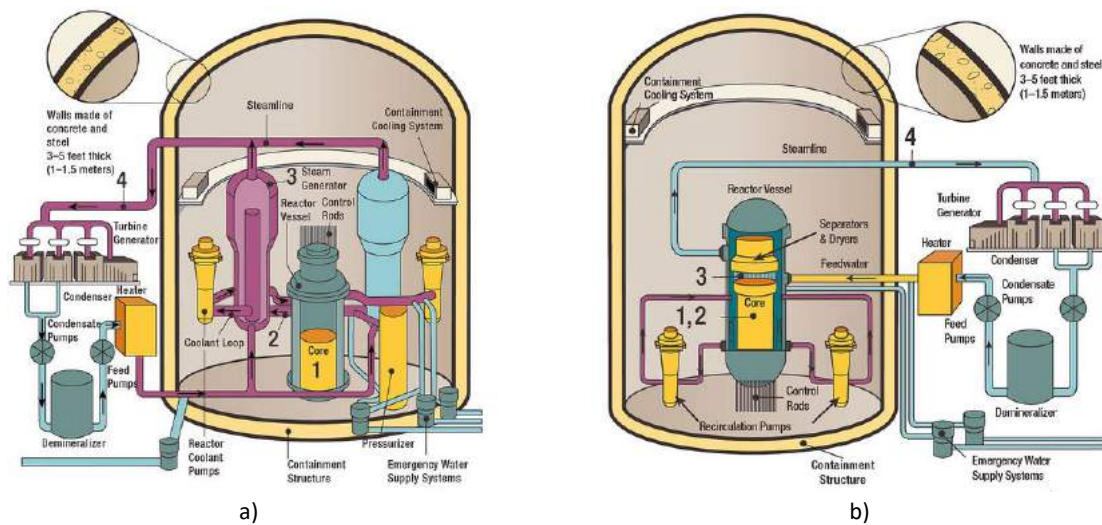
Figure 2-1: Schematic representation of a pressurized water reactor (a) and a boiling water reactor (b) (Source NRC).

2.2 ZIRCONIUM ALLOYS IN THE NUCLEAR INDUSTRY

2.2.1 FUEL ASSEMBLIES

As anticipated in the previous section, the fuel of choice for LWRs is UO_2. The urania is used in the form of pellets, the pellets are piled vertically inside 4 m long cladding tubes made of zirconium alloys. Typically, Zircaloy-2 is used for BWRs, and Zircaloy-4, M5 or ZIRLO are used for PWRs, see Table 2-1 for the alloys' composition. The cladding diameter is approximately 10 mm, while the cladding wall thickness can vary between 0.6 and 0.8 mm. Multiple tubes are stacked together using spacer grids, guide tubes and end plugs in arrays of 10x10 for BWRs and 14x14 or 17x17 in PWRs, forming a fuel assembly. An example of a fuel assembly is displayed in Figure 2-2. Up to 800 assemblies can be found in a BWR core and 150-300 assemblies for a PWR reactor, amounting to 25-40 tonnes of zirconium in a LWR core [5,6]. The fuel assembly is designed to allow water or steam to flow through the fuel without the insurgence of turbulences allowing the cooling of the core, and extracting effectively the heat from the fission reaction in order to drive the steam turbine. The cladding is fundamental in keeping the urania and the water apart, while containing any fission product and avoiding the possibility of radioactive species ending up in the coolant. Efficient heat transmission across the cladding wall is necessary for the heat generated inside the pellet to escape into the water. The cladding needs to withstand its own weight, it has to be able to contract inwards at the beginning of its fuel cycle to accommodate the in-reactor pressure, and to expand in later stages to follow the swelling of the fuel pellets. All these requirements dictate minimum mechanical strength and good ductile creep behaviour. Additionally, to maintain a sustained fission reaction, any cladding material needs to have very low adsorption of thermal neutrons.
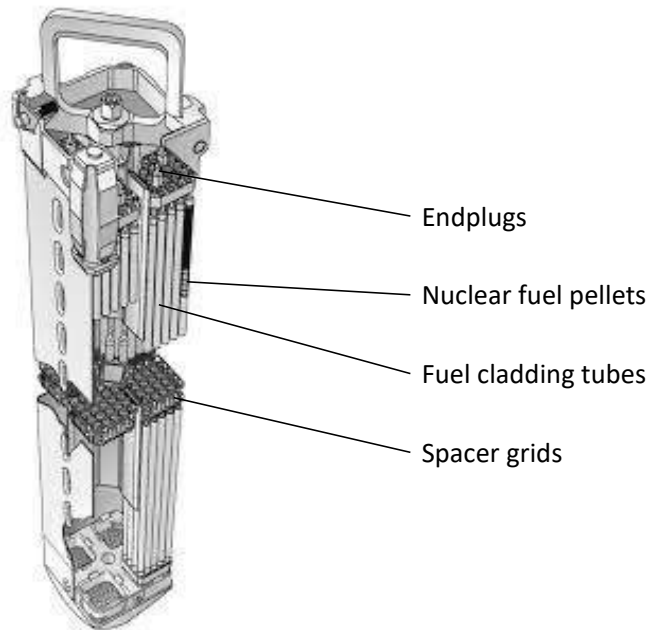
Figure 2-2: Schematic representation of a BWR fuel assembly and its components (courtesy of Westinghouse Electric Sweden)

2.2.2 ADVANTAGES OF ZIRCONIUM

During the first deployment of commercial nuclear power plants in the 1950s, steel was selected as cladding material, while zirconium was deemed too expensive and its use was limited to submarine reactors. By the mid-1960s though, the price of zirconium decreased enough to allow its use for civil power generation, and most commercial reactors switched from austenitic steels to zirconium alloys. The main reason for this change was the very low thermal neutron cross-section of Zr, which is of fundamental importance for the neutron efficiency and overall neutron economy inside the core. Zirconium is virtually transparent to thermal neutrons (which are the most likely ones to produce a fission event in the fuel) allowing them to travel through the cladding, which is key in maintaining the fission reaction. Pure zirconium, though, has poor mechanical properties and low resistance to corrosion. For this reason, the aforementioned Zr-alloys were developed. Their mechanical properties were improved through solid solution hardening induced by Sn and by the precipitation of second phase particles, SPPs. Corrosion resistance was greatly improved by the addition of Fe, Cr and Ni [7]. Heat treatments and careful forming are also important in providing optimal properties. For example, Optimized ZIRLO™ claddings are produced with a fabrication process that involves forging of a billet, homogenization quenching of the billet, extrusion of the billet into an extruded tube, followed by an annealing. The extruded tube is then reduced to the final thickness and diameter by alternating pilgering and annealing steps. Finally, a PRXA heat treatment is used to produce the desired isotropic partially recrystallized microstructure [8]. This microstructure is characterized by the presence of larger grains (3-5 µm in size) surrounded by smaller sub-micron grains.

As a result of the finely tuned chemistry and microstructure of the claddings, the materials currently used perform well under normal operating conditions and most of the degradation mechanisms that affect zirconium alloys inside the core of a LWR are reasonably understood and controlled. One degradation mechanism that still occurs in operating reactors is debris fretting of the cladding tubes. In debris fretting, a foreign debris carried by the water gets trapped between the cladding tube and the spacer grid. When in this position, the water flow keeps moving the debris against the cladding tube resulting in wear and abrasion of the cladding. This phenomenon can even result in cladding perforation and it is the most common cause of rod failure [5,9].

Table 2-1: Chemical composition of some of the mostly used zirconium alloys.

Alloy	Composition (wt%)						
	Sn	Fe	Ni	Nb	Cr	O	Zr
Zircaloy-2	1.2-1.7	0.07-0.20	0.03-0.08	-	0.05-0.15	0.125	balance
Zircaloy-4	1.2-1.7	0.18-0.24	-	-	0.07-0.13	0.125	balance
M5	-	<500 ppm	-	0.8-1.2	-	0.125	balance
ZIRLO	1.0-1.1	0.09-0.10	-	1.0-1.2	-	0.125	balance

2.3 ACCIDENT TOLERANT FUELS

2.3.1 AN OPPORTUNITY FOR NEW MATERIALS

The concept of ATFs has emerged as response to the Fukushima Daiichi accident in 2011. In this unfortunate accident, the impossibility to pump cooling water into some of the reactors in the plant triggered an increase in the core temperature beyond the design conditions. This type of accident is generally referred to as loss of coolant accident (LOCA). Under these conditions the temperature in the core can rapidly rise to 700°-900°C. At this temperature the oxidation rate of the zirconium in contact with hot steam can drastically increase. As the reaction is exothermic, it can cause further temperature rise and it can trigger an autocatalytic exothermic oxidation reaction. This chemical reaction, expressed in Equation 2.1, results in the transformation of the cladding tubes into ZrO_2 and in the production of ignitable H_2 gas.

$$Zr(s) + 2H_2O(l,v) \leftrightarrow ZrO_2(s) + 2H_2(g) + Heat\ of\ reaction \qquad (2.1)$$
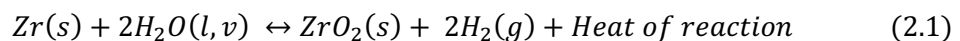
The oxidized claddings lose most of their integrity and mechanical strength, the fuel pellets and fission products are let into the water, the large amount of generated hydrogen builds up pressure in the core and any leak of this gas can result in large explosions. Considering that there are between 25 and 40 tons of zirconium in a LWR core and that this runaway reaction can take place in a relatively short amount of time (~2h [10]), the severity of this accident scenario becomes immediately clear.

The accident at the Fukushima Daiichi power plants shook the nuclear industry. Nuclear electricity production had stagnated from the 1990s to the 2010s, especially in western countries, and this accident represented an additional obstacle for any further growth of this technology. In the years following the accident, many nuclear power plants were shut down, especially in Europe, and it was clear that the nuclear industry had to invest in innovation and safety if nuclear was to be considered again a viable technology for the decades to come. Parallel to this, governments and international energy agencies started to pay more attention to other fossil-free energy sources, with the green revolution acquiring momentum. Nuclear energy is not a renewable source of energy, but it has the advantage of having an extremely low carbon footprint and of being independent from weather conditions. These two features make nuclear energy a valuable technology to be coupled with wind, solar and hydro in the attempt to move away from fossil fuels. The possibility of nuclear energy being part of the solution to climate change and the unfortunate Fukushima accident created the perfect conditions for a wave of renewal for this technology, driving a great amount of research focused on improving current designs and creating new ones.

Accident tolerant fuels aim at creating a better technology for nuclear energy production through the improvement of existing LWR based designs. The research on ATFs is divided into two main groups, improvements of the fuel pellets and improvements of the cladding tubes. When dealing with the cladding tubes, the main objectives are to avoid the repetition of a Fukushima-like accident by delaying, or making it impossible, the runaway oxidation of the Zr, and to improve the cladding performances under normal operation providing more flexibility and increased fuel lifetime. In order to achieve these objectives, both near-term and long-term solutions are being investigated. For the near term, the application of a thin, corrosion resistant coating on the outer surface of the currently used zirconium cladding is the main stream of work. The solutions for the long term aim at the integral substitution of the Zr cladding from the core, the two main designs that are being considered are FeCrAl alloys and SiC/SiC composite materials. Since changing any parameter inside a LWR core would inevitably change the neutron economy and the reactor physics, it is important to consider the research on the fuel pellets and on the claddings as complemental. A schematic of the research organization around the concept of ATFs is presented in Figure 2-3 [6,11].
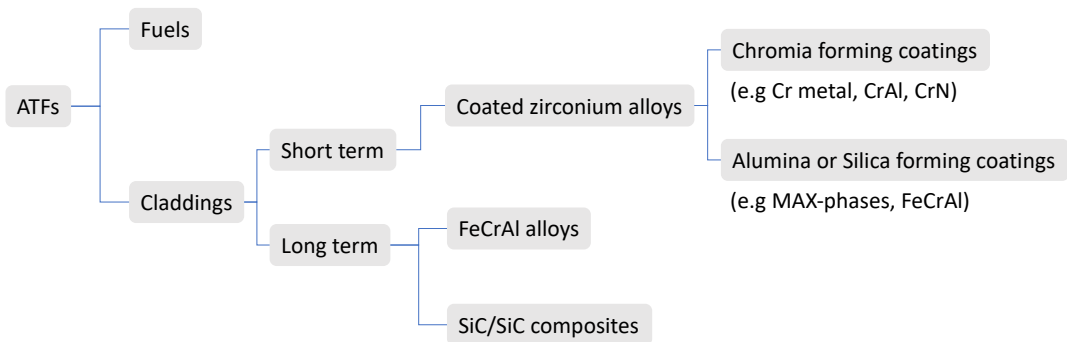

Figure 2-3: Organization of the global research on accident tolerant fuels.

2.3.2 COATED ZIRCONIUM CLADDINGS

The main reason why the application of a thin coating is compelling is that it would have little or no effect on the properties of a standard Zr-based cladding and it would not influence excessively the core neutron economy. Thin coatings would not change the core physics too much and might even result in better overall performance while providing longer coping times in case of a severe accident. Beyond the improved performance under accident conditions, increased debris fretting resistance is one of the main expected advantages that a coating could provide. Adding a step in the production process of the cladding tubes is expensive and it would result in a higher fuel cost. Improved debris fretting resistance would reduce the number of times the production of electricity in the plant needs to be stopped to perform rod maintenance, partly compensating for the higher production cost of the fuel. The only drawback of this approach is that Zr is still kept inside the core. It is true that the outer diameter of the cladding would be protected from oxidation, but under LOCA conditions the rapid increase in temperature can simultaneously cause build-up of pressure in the tube and deterioration of the mechanical properties of the cladding, often resulting in ballooning and bursting. Once a cladding has burst, the steam has a path to get to the inner surface causing Zr oxidation and making the coating partly ineffective. Nevertheless, the oxidation of an uncoated Zr cladding from the outer diameter is one of the co-causes of cladding ballooning and bursting: since severe Zr oxidation causes strong impoverishment of the mechanical properties of the cladding, the more oxidized the cladding becomes the weaker and more likely to burst it gets. In conclusion, the application of a thin coating would not be an infallible solution but it is generally deemed to be able to significantly delay the complete failure of a traditional Zr cladding under severe accident conditions. [12]

As shown in Figures 2-3, two main families of coatings are being investigated: chromia forming coatings, and alumina or silica forming coatings. Among the chromia forming coatings, metallic Cr has been studied profusely as ATF solution for PWRs. Metallic Cr is selected because it forms a passivating and dense scale of chromia when exposed to water corrosion. This oxide scale is impermeable to oxygen and it stops or slows down significantly the oxidation process. Dissolution of chromia in water is possible and its rate depends on temperature and chemical environment. Overall, chromia growth and dissolution are the main factors determining if the coating is going to be consumed or if the system stabilizes once an initial protective scale is formed [13–15]. In experiments, Cr-coatings on Zr-claddings have resulted in lower oxidation rates, reduced hydrogen pickup, enhanced resistance to debris fretting and improved mechanical properties of the cladding in PWR environment [16–22]. Under simulated accident conditions, Cr coated claddings have exhibited smaller ballooning sizes and significantly improved high temperature steam oxidation resistance [4,23,24]. All the properties demonstrated by metallic Cr makes it one of the best candidates as near-term ATF for PWRs. Cr coatings can be deposited with different deposition technologies, the main coating that are being developed are deposited with physical vapour deposition or CS deposition.

COLD SPRAY DEPOSITION TECHNOLOGY

Cold spray is a technology employed for coating deposition, additive manufacturing, and in-situ component restoration. This technique was initially developed in the mid-1980s at the Russian Academy of Science in Novosibirsk [25] and it is part of a wider group of thermal spray techniques and it is characterized by low particle temperatures and high particle velocities as displayed in Figure 3-1. Unless specified otherwise, this chapter's references are [26,27].
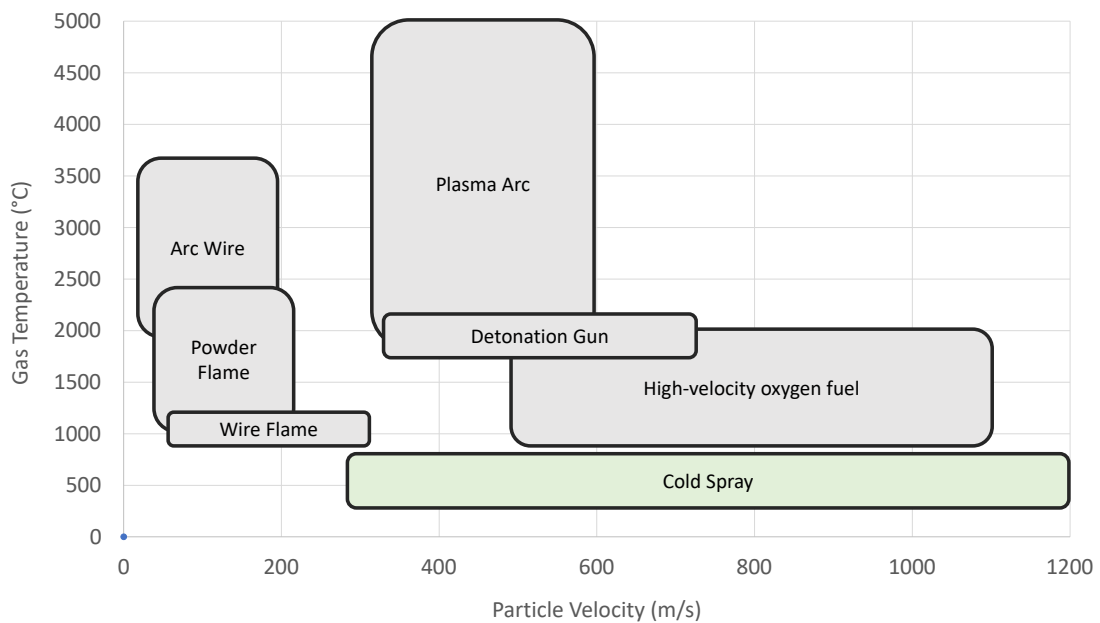

Figure 3-1: Comparison of particle speed and gas temperature in cold spray and other thermal spray processes (Reproduced from [27]*).*

3.1 WORKING PRINCIPLES OF COLD SPRAY DEPOSITION

In CS deposition particles from a feedstock powder are used to form a coating on a substrate. The deposition process is based on accelerating the particles up to supersonic velocity and directing this jet of particles onto the substrate. The coating is built particle by particle via ballistic collision between the particle and the substrate and/or other previously deposited particles. The particle size is usually ranging from a few micrometres up to 100 μm, the achieved particle velocity can reach 1500 m/s, but is more typically varying between 300-1200 m/s. To accelerate the particles up to these speeds, the powder is fed to a high-pressure gas stream, the gas stream is let through a converging-diverging nozzle that allows the gas to expand and cool down increasing its speed to supersonic velocities together with the powder. A schematic description of a cold spray deposition set up is displayed in Figure 3-2. High-pressure gas is supplied to a gas heater where the gas temperature is increased to 100-800°C. Then the gas stream is let through the nozzle where it expands and accelerate to form the

supersonic gas jet. The same high pressure gas supply is used to create a separate gas stream that transports the feedstock powder to the main gas jet. The powder is typically fed to the main gas jet before the nozzle, but there are systems where the powder is injected in the nozzle after the nozzle throat. The mix of hot, high-pressure gas and the powder, accelerates through the nozzle and the particles are sprayed onto the substrate at high velocities. Particle adhesion and coating formation is achieved upon high velocity collision with the substrate. During the collision, particles and substrate are subjected to high rate, high strain plastic deformation that is at the origin of particle adhesion and coating formation. Due to this fact, a certain degree of ductility of the particles and the substrate is needed. This requirement on ductility makes it challenging to use ceramic powder as feedstock material, composite ceramic coating where one ductile material is coupled to a hard material is possible. However, metals remain the most commonly material family employed as feedstock powder for CS deposition. Thermoplastic polymers are also a feasible powder option of polymeric coatings [28]. The name *cold* spray technique comes from the fact that the temperature of the final powder/gas supersonic jet is usually below a few hundred degrees Celsius.
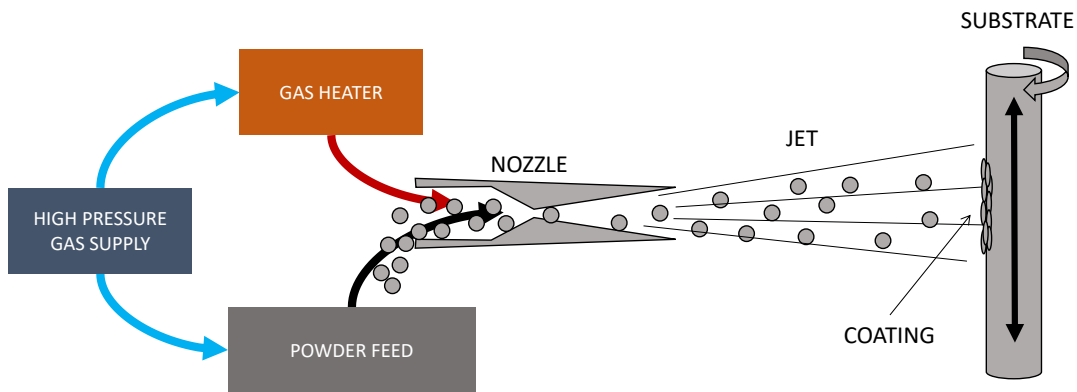

Figure 3-2: Schematic representation and basic working principle of a cold spray setup.

3.2 Advantages and Disadvantages of Cold Spray Deposition

As shown in Figure 3-1, the main differences between CS and other thermal spray techniques are the lower temperature of the gas jet and the higher particle velocities. The low temperatures involved in this deposition method, plus the use of an inert gas, lead to a strong advantage of CS: no significant phase transformation or oxidation processes occur on the particles or on the substrate during the deposition. Additionally, the thermal input on the substrate is minimal, making CS deposition suitable for temperature sensitive materials with little effect on the substrate microstructure. The content of oxygen in the final coating can be even lower than the oxygen content of the starting powder material. Each particle has a thin native oxide layer, as the particle impacts with the substrate the oxide shatters and detaches from the particle and gets flushed away by the gas jet [29,30]. Then, the exposed bare metallic surface of the particle bonds with the surrounding particles or substrate. As a secondary effect of this intimate interparticle contact, the electric conductivity of CS metallic coatings is typically

extremely high. In addition, CS coatings retain the chemical purity of the base material and this can be an advantageous in preserving the good corrosion resistance characteristic of certain metals. The other fundamental characteristic of CS is the high particle velocities involved in the deposition process. The high particle velocities together with the velocity distribution (which results in some particles moving below the critical particle velocity) produces a triple effect of grit blasting, spray coating and shot peening, where the substrate surface is prepared, loosely attached particles are removed and the coating is made denser. Summing up all effects, including the high degree of plastic deformation involved in the coating formation process, the result is a dense coating, with significant compressive residual stresses, with small grain size, high hardness, high strength, and with no grain growth induced in the substrate or in the coating. Anyhow, there are some disadvantages. As-sprayed coatings have almost no ductility left. Due to the nature of CS, the adhesion is strongly linked to plastic deformation. A degree of plastic deformation of the substrate is expected in order to have good adhesion, and as a consequence, CS coatings on ceramic substrates have limited bonding strength. To achieve a high particle velocity, light molecular weight gases are used. Helium is commonly used but it is a limited resource and the application of this technique on a large scale using this gas is problematic. Moreover, it can be challenging to coat complex shapes or large areas because the spray beam is usually relatively small (10 mm in diameter) and it must be kept at a short fixed distance from the substrate for optimal coating formation [31].

3.3 COLD SPRAY PROCESS PARAMETERS

The working principle and the schematic of the CS setup are quite simple. Nevertheless, to achieve particle adhesion and to obtain the desired coating properties, many different parameters need to be optimized. In this section, the most important parameters involved in CS deposition are listed and the effects of tuning these parameters are explained.

3.3.1 POWDER SIZE, SHAPE AND PROPERTIES

The properties of the feedstock powder have a direct effect on the resulting coating properties. Powder size, shape, microstructure and material properties all have important consequences on the CS process. These properties can be controlled to a certain degree but are also strongly affected by the powder manufacturing process and by the material selected for the coating. Common powder manufacturing processes are gas atomisation and ball milling, these methods provide spherical particles and flake-like powders, respectively. Subsequent processes as flame treatment, sintering and friction welding can be used to agglomerate the obtained particles in larger sized particles or composite particles. Sponge-like and porous particles can also be manufactured. The shape of the particles can have an effect on the final particle velocity: irregularly shaped particles achieve higher velocities than spherical particles [32]. Particle density and porosity can be used to control the density and porosity of the deposited coating. Once produced, the powder size distribution can be controlled through sieving. The particle size is particularly important for the achieved particle velocity, smaller particles will be accelerated faster by the gas jet but will slow down earlier than bigger/heavier particles once they leave the nozzle. It is easier to achieve high particle velocities with finer particles, but the use of finer particles will require shorter spray distances [33]. The particle size distribution and maximum dimension will also influence the final microstructure of the deposited coating. The

species selected as material for the particles are also of fundamental importance, the choice of the material is clearly influenced by the final intended application of the coating, but different materials have different mechanical properties and will behave differently upon impact during CS deposition. Finally, the particle microstructure can influence particle hardness and final properties of the obtained coating. Powders obtained with atomization are often characterised by very small sub-particle grains, a fine grain size leads to higher hardness and reduced ductility. For the same reason, annealing the feedstock powder before use in CS is usually associated with a higher degree of ductility of the powder and better deposition efficiency [32,34]. The presence of an oxide layer on the surface of the particle can also have consequences on the particle adhesion and on the final conductivity of the coating. Scanning electron microscopy (SEM) images of the feedstock powder used in this study are presented in Figure 3-3.
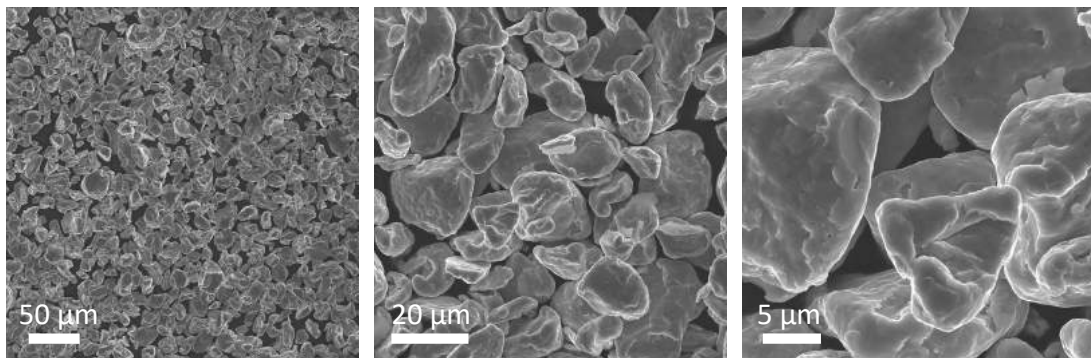

Figure 3-3: SEM images of pure Cr powder employed in the deposition of cold spray Cr-coatings.

3.3.2   PARTICLE VELOCITY AND TEMPERATURE

Particle start? velocity and the velocity at which the particles impact the substrate are the most important factors for the successful formation of a cold sprayed coating. The adhesion of the particles to the substrate involves high strain and high-rate plastic deformation in both particle and substrate. Below a certain particle velocity, the impact energy can be insufficient to produce such deformation and to achieve good adhesion. The velocity threshold at which coating adhesion and formation start to become significant is called the *critical particle velocity*, this velocity is characteristic of each coating/substrate system and the relationships between critical particle velocity and adhesion will be explored in a following section. The main means of controlling the achieved particle velocity is by controlling the velocity of the gas in the supersonic jet formed after the nozzle. Particle size, density and shape can influence the coupling between the gas flow and the powder, but the gas jet velocity represents both the driving force for particle acceleration and the maximum obtainable particle velocity. The equation of the speed of sound in a gas is given by:

$$v = \left(\frac{\gamma RT}{M_w}\right)^{\frac{1}{2}}$$ (3.1)

Where γ is the ratio of the specific heats, R is the gas constant, T is the temperature of the gas and M_w is the molecular weight of the gas. When the gas velocity at the nozzle throat reaches the speed of sound, the flow is chocked and any increase of pressure in the gas feed will have

no effect on the velocity of the gas after the nozzle. Because of this, increasing the pressure of the feed gas beyond a certain level will not result in increased gas velocity, the most common way to increase the gas velocity is to increase the upstream gas temperature or to use a gas with lower molecular weight (for example He). The final gas velocity is obtained when the heat energy of the gas flow is converted into kinetic energy during the downstream expansion of the gas. Increasing the gas temperature can also result in heating of the sprayed powder. The heat transfer depends on many factors but is generally considered positive for coating formation as yield strength, hardness, shear modulus and other material properties are influenced by temperature. Higher particle temperature could increase the ductility of the powder material, reducing the amount of kinetic energy required to produce the plastic deformation needed for coating formation, hence lowering the critical particle velocity. Clearly, being a *cold* deposition technique, particle temperature cannot be brought up to near melting temperatures and it is usually kept far below this threshold, however, particle temperature remains a relevant parameter in CS.

3.3.3 OTHER IMPORTANT PROCESS PARAMETERS

All the parameters previously discussed assumed fixed nozzle design and did not take into consideration any of the deposition strategy parameters. The formation of the gas jet, though, is strongly influenced by the design of the nozzle. Different nozzle designs exist but the convergent-divergent nozzle seems to allow for higher achieved particle velocities and it is the most commonly used nozzle in CS deposition. Nozzle material is also a relevant factor, to avoid contamination from the nozzle into the deposited coatings. Also, the nozzle must resist the wear and abrasion induced by the flow of the powder particles. For this reason, hard materials such as tungsten carbide are usually preferred. Once every other parameter has been fixed and the characteristics of the jet of particles are determined, deposition strategies and parameters can affect the resulting CS coating. Nozzle traverse velocity influences the deposited coating thickness for each passage. Spray distance influences primarily the velocity of impact of the particles: the particles are accelerated while in the gas jet, but start decelerating when interacting with the ambient air resistance, for longer spray distances the deceleration in air increases in importance. Additionally, the spray distance can affect the shape of the bow shock wave that forms when the gas jet interacts with the substrate, this shock wave can slow down the particles, affecting the deposition process. Spray angle is linked to the particle normal velocity relative to the substrate surface. When spraying at an angle, the tangential component of the particle velocity can cause detachment of loosely attached deposited particles. The scanning step distance affects the overlap between different sprayed tracks and can result in different coating profiles. Finally, substrate surface preparation can greatly influence the interaction between the sprayed particles and the substrate, affecting deposition efficiency and rate.

3.4 BONDING PROCESS AND ADHESION IN COLD SPRAY DEPOSITION

The basic principle for CS coating formation is the transformation of the particle kinetic energy into extensive plastic deformation upon collision with the substrate. The extreme plastic deformation disrupts the thin native oxide layer present on the particle surface and exposes new bare surfaces to the elevated contact pressure that results into an intimate contact between clean surfaces. Plastic deformation appears to be central in the formation of a strong bond during CS deposition. To sustain this hypothesis, a certain degree of ductility is a prerequisite for successful adhesion of the coating, and non-ductile materials as ceramics can be deposited only together with a ductile material. Moreover, the fact that a minimum particle critical velocity needs to be achieved in order to obtain particle adhesion seems to suggest that a minimum amount of kinetic energy is required to produce the needed plastic deformation in the particle. Still, the mechanisms by which the strong bond between different particles and between particles and substrate forms is still not completely understood [35].

The main phenomena that are believed to affect adhesion in CS are plastic-flow localization and adiabatic shear instability. Plastic deformation always results in heat production, under normal conditions, though, the heat production rate is not high enough to generate a significant increase in temperature, so heat can dissipate and the material deforms under isothermal conditions. In the case of CS, the duration of a particle collision event is usually under a few hundred nanoseconds [36,37]. Under these conditions the heat generated by the plastic deformation has no time to dissipate. The temperature increases locally causing softening and annealing of the work-hardened material, resulting in a decrease of the stress needed to produce further plastic deformation. As a consequence, if some regions end up being subjected to more plastic deformation than others, these regions will be softened more and will become more prone to accommodate further deformation, giving rise to plastic-flow localization. When plastic-flow localization occurs, shear and heat production become strongly localized in some regions while other parts of the material are subject to little or no deformation. In CS deposition, the periphery of each particle is subjected to the highest degree of plastic deformation and heating, here the temperature can rise significantly (even up to 0.99 T_m [38]), while the bulk of the particle experiences little deformation [38,39]. Figures 3-4 (a) display the different stress-strain curves for materials subjected to isothermal deformation, adiabatic deformation, and localized-adiabatic deformation. Additionally, a schematic of the different deformations resulting from adiabatic and localized-adiabatic condition are shown in Figure 3-4 (b) and (c).
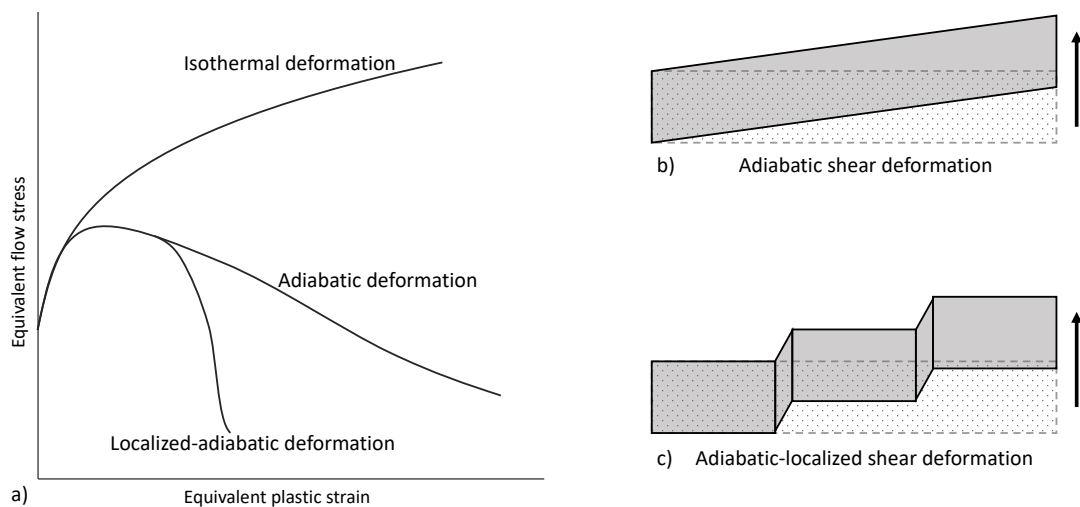
Figure 3-4: (a) Schematic stress-strain curves for isothermal, adiabatic and adiabatic-localized plastic deformation. (b) and (c) Comparison between adiabatic shear deformation and adiabatic-localized shear deformation, respectively. (Reproduced from [35]*)*

Despite reaching temperatures close to the melting temperature, due to the extremely short duration of the collision event, surface melting and atomic diffusion across the interface do not seem to be the main actor in the formation of a strong bond. Two processes, acting respectively at particle-size length-scale and at nanometre length-scale are commonly assumed to be responsible for the strong adhesion. At the particle-size length-scale, the substrate is commonly reported to significantly deform wrapping around the incoming particles, resulting in mechanical interlocking between particles and substrate (See Figures 3-5). In this topological arrangement, the particle would be geometrically locked into place even without any strong interfacial adhesion between coating and substrate. To explain the strong bonding at the nanometre scale, instead, the concept of interfacial instability is often used. Interfacial instabilities can arise when two fluids flow at different velocities parallel to their shared interface, and can result in the formation of interfacial roll-ups and vortices. If the periphery of the sprayed particles is assumed to undergo a phenomenon of strongly localized adiabatic plastic deformation, the behaviour of these regions could be described as fluid-like. Being fluid-like, the material at the interface with the substrate (or with other particles) could be affected by the phenomenon of interfacial instability, with consequent formation of nano-scale roll-ups and vortices. The formation of these structures could be one of the mechanisms behind the strong adhesion of CS coatings. Overall, these mechanisms seem to play a role in the adhesion of CS coatings and depending on the properties of the different coating/substrate systems, one mechanism can be predominant over the other.
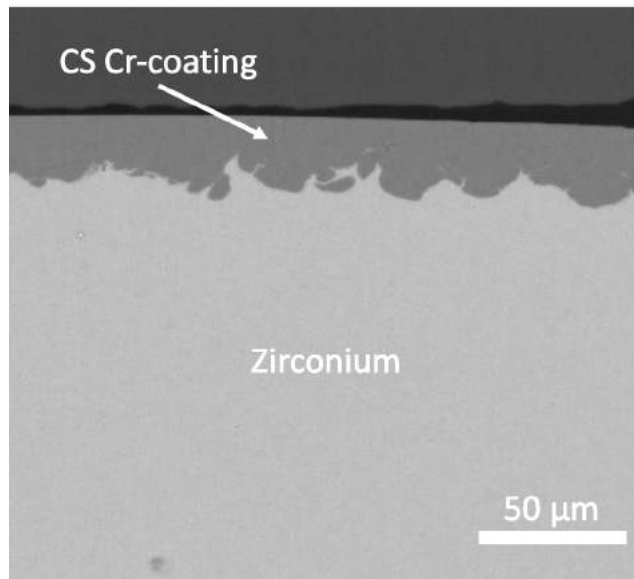
Figure 3-5: Cross-sectional SEM image of cold spray Cr-coating on a Zr-alloy substrate.

EXPERIMENTAL PROCEDURES

4.1 MATERIALS

Cold spray Cr-coated Optimized ZIRLO cladding tubes were the focus of this work. Two different version of as-fabricated claddings and one set of autoclave exposed claddings were provided by Westinghouse Electric Company. For the as-fabricated samples, the two coatings were deposited to a thickness of 100 μm and 50 μm, respectively. The coatings were subsequently ground down to a final thickness of approximately 50 μm and 20 μm. The 50 μm thick version of the coating represents an early prototype of the final product, which is represented by the 20 μm thick version. The 20 μm version was then selected for autoclave exposure. The list of the available samples can be found in Table 1. An image of the as-fabricated coated cladding sample is presented in Figure 4-1.

Table 4-1: List of analysed samples.

Samples	Conditions	Deposited coating thickness	Final coating thickness	Development stage
A1	As-fabricated	100 μm	50 μm	Prototype
A2	As-fabricated	50 μm	20 μm	Final version
B2	Autoclave exposed	50 μm	20 μm	Final version

As-fabricated Cr-coated Optimized ZIRLO™ cladding
200 mm length, 9 mm ∅, 0.6 mm thickness

Figure 4-1: Photo of as-fabricated Cr-coated Optimized ZIRLO™ cladding sample

The coatings were obtained by the deposition of pure Cr feedstock powder sieved to a size smaller than 44 μm. The cladding tubes used as substrate for the coating were made out of Optimized ZIRLO (OPZ) alloy (0.8-1.2 wt.% Nb, 0.6-0.79 wt.% Sn, 0.09-0.13 wt.% Fe, 0.09-0.16 wt.% O, balance Zr). The achieved particle velocity during deposition was of 1200 m/s (+/- 50 m/s).

The autoclave exposure was conducted at Sandvik Materials Technology for 90 days at 415°C in water with PWR chemistry [40]. Images of the autoclave setup are presented in Figure 4-2.

Figure 4-2: The autoclave setup: the autoclave (left), the top without cover (centre), the inside (right).

4.2 CHARACTERIZATION TECHNIQUES

4.2.1 SCANNING ELECTRON MICROSCOPY

Scanning electron microscopy is one of the most widely used imaging techniques in science. SEM can be used on almost any material. It allows to obtain both topological and chemical information from the samples and the most modern instruments have achieved nanometre resolution. It is flexible and can be used on bulk sample surface, cross-sections, particles, films, etc., with very little or no sample preparation. References for this section are [41,42].

The generic functioning of an SEM is schematically shown in Figure 4-3. In an SEM, electrons are extracted from an electron source by the use of strong electric fields (and heat in the case of thermo-ionic guns). The two main types of electron guns are thermo-ionic guns (not used in modern SEMs) and field emission guns (FEGs). The extracted electrons are accelerated towards the anode by an electric field, the achieved energy of the obtained electron beam ranges usually between 2 keV and 30 keV, although voltages as low as 0.1 keV can be used. Electromagnetic lenses are used to converge the beam into a fine probe, in this sense the SEM is a demagnifying instrument and the electron-probe is the projection of the electron source reduced in size. The e-beam is then let through the condenser aperture which determines the convergence angle of the probe. Scanning coils are used to deflect the beam path allowing to scan the probe on the surface of the sample. When the electron probe hits the sample surface, different interaction phenomena between electrons and matter will take place and different types of signals will be emitted from the sample surface. The typical signals produced in the electron-matter interaction volumes are Auger electrons (AEs), secondary electrons (SEs), back scattered electrons (BSEs) and characteristics X-rays. The signals will be collected by different detectors and associated with the position of the e-beam, the e-beam will then be moved to the next region by the scanning coils and the process will be repeated. As displayed in Figure

4-3, each signal can originate from a pear-shaped region called the interaction volume. The primary factors determining size and shape of the interaction volume are the probe size and the beam energy, larger probes will shower a wider portion of the sample surface, plus the higher the energy of the electrons in the e-beam the deeper the electrons will be able to penetrate into the material. Additionally, different signals travel different distances through the sample before being reabsorbed, hence any signal produced at a distance from the surface longer than its mean free path will not be able to leave the sample and will not be detected, this determines the escape depth of each type of signal. All these effects are also influenced by the material composition that can greatly affect the escape depth and the size of the interaction volume.

SEs, generated when the incident beam excites outer shell electrons of the specimen atoms, have energies below 50 eV and can be easily be reabsorbed by the sample. They have a shallow escape depth, which makes this signal very localized around the area immediately underneath the electron probe (few nanometres under the surface). SEs are usually detected by an Everhart-Thornley detector, more recent instrument are also equipped with an InLens detector. This signal provides important topographic information, have high spatial resolution and can be used to produce images based on morphological contrast. BSEs are electrons from the primary beam that have been scattered by the interaction with the atomic cores of the sample and have been deflected backwards. These electrons have significantly higher energies than SEs and have larger escape depth. For this reason, this signal has lower spatial resolution. BSEs are collected by a BSE detector and can provide elemental information in the form of Z-contrast. The local average atomic weight is the main factor determining the likelihood of elastic scattering interaction that results in the emission of BSEs. Elements with higher Z will result in brighter BSE images. When the electron beam interacts with the sample atoms, an electron from an atom core shell can be ejected from the atom. When this happens, an electron from a higher energy level will quickly make the transition downwards to fill the vacancy. In most cases, this transition will be accompanied by an emitted photon (X-ray) whose energy matches the energy gap between the upper and lower level. In other cases, the energy released by the downward transition is given to one of the outer electrons instead of to a photon. This electron (i.e, AE) is then ejected from the atom with an energy equal to the energy lost by the electron which made the downward transition minus the binding energy of the electron that is ejected from the atom. AEs have very low energy and can travel only few atomic layers, they need ultra-high vacuum to travel undisturbed, they cannot be collected in a standard SEM. X-rays can typically travel very far into materials, so they can reach the surface even when produced deep underneath the sample surface causing lower spatial resolution than any electron signal. These characteristic X-rays are collected by an energy dispersive spectroscopy (EDS) detector and they are used to extract qualitative and quantitative chemical and compositional information about the specimen.

In this work, FEI Quanta 200 FEG Environmental SEM (ESEM) and a JEOL 7800F Prime SEM were used to capture images of the coated cladding cross-sections and to perform EDS mapping of the same areas.
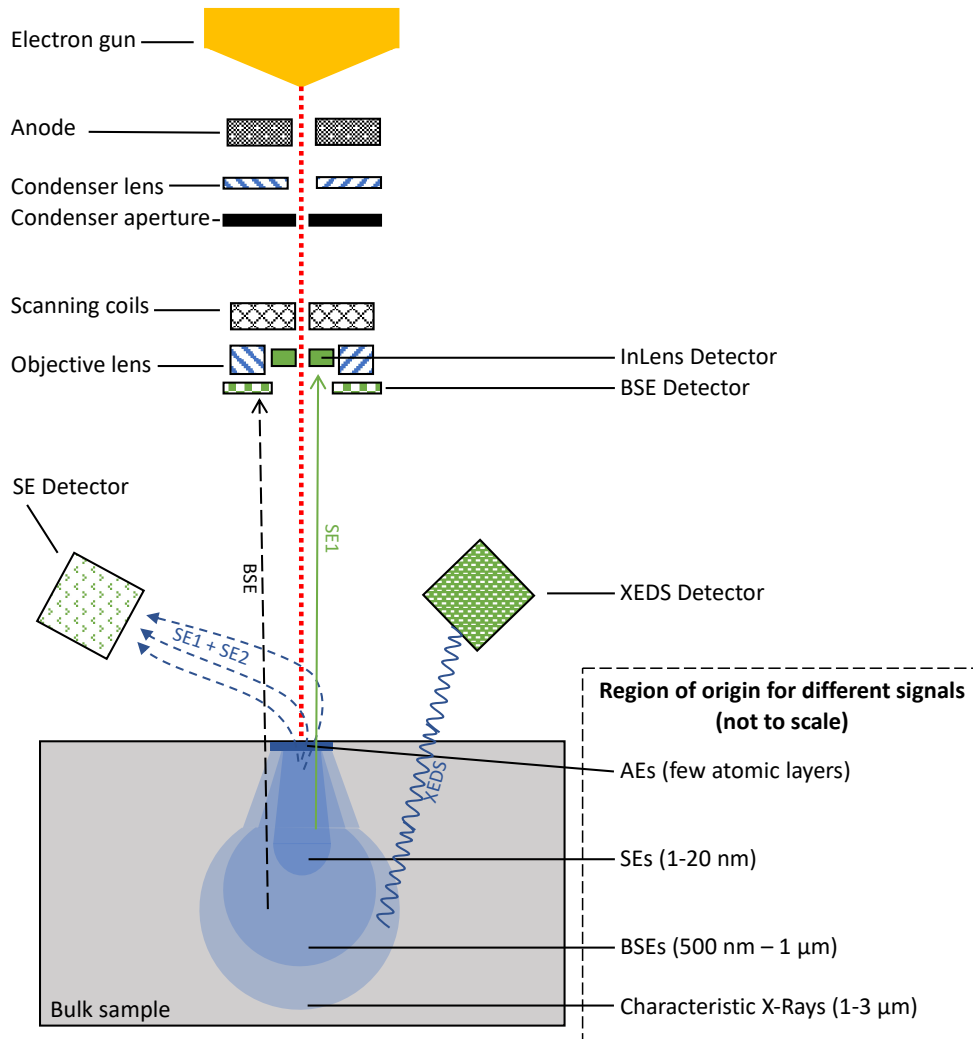
Figure 4-3: Schematic diagram of SEM. Instrument, e-beam/sample interactions and the origin of the different signals.

ELECTRON BACKSCATTERED DIFFRACTION AND TRANSMISSION KIKUCHI DIFFRACTION

Electron backscattered diffraction (EBSD) and transmission Kikuchi diffraction (TKD) are both SEM based techniques where the scattered electrons emitted by the sample are used to investigate the type and orientation of the specimen crystal structure. These techniques provide a powerful tool to read into the microstructure of the material. The main limitation of EBSD and TKD is the sample preparation: in order to be able to collect the signal, the surface quality needs to be extremely good and with some materials it can be challenging to achieve this result. References for this section are [43].

When an electron beam interacts with matter, some of the electrons originated from the primary beam will be scattered. Scattering occurs through both elastic and inelastic events and a single electron can be scattered many times. Under the flux of primary electrons, scattered electrons are constantly generated in the interaction volume and are emitted in all directions.

20

To leave the sample, these electrons have to move through the crystal lattice, being originated from the entirety of the interaction volume and emitted in all directions, some of them will be travelling at an angle to a lattice plane that meets the Bragg's law and will be scattered following the Bragg's law. If the last scattering event of an electron before leaving the sample fulfils the Bragg condition, this scattering event will create a deficient region (where the electron should have gone otherwise) and an excess region (where the electron has been scattered towards) in the incoherently scattered electrons' distribution (originally uniform). When many of these events are added together an excess line and a deficient line will appear in the incoherently scattered electron distribution, these lines are called Kikuchi lines and a pair of Kikuchi lines produces a Kikuchi band. Being produced by Bragg diffraction, the position of these bands is strictly associated with the orientation of the crystal lattice and influenced by the crystalline structure and the lattice plane distance. When this signal is collected from a bulk sample the technique is called EBSD, when these patterns are obtained in transmission from a thin sample the technique is referred to as TKD, a schematic for EBSD and TKD setups is reported in Figure 4-4. In EBSD the sample is typically tilted to 70° to maximise the amount of signal hitting the detector. On the other hand, but for the same reason, in TKD the sample is usually tilted to -20°. The Kikuchi patterns from each scanned point are collected by an EBSD detector and automatically indexed by a computer system via comparison with a database. The crystallographic data can then be analysed and used to produce band contrast maps, orientation maps, pole figures and more advanced analysis of grain deformation, strain, etc.

EBSD and TKD were employed to study the crystal and grain structure of the CS-Cr coating and of the OPZ substrate. To access this information, EBSD was performed on polished cross-sections and TKD was utilized on TEM lamellas. EBSD and TKD mapping was performed on a TESCAN GAIA3 equipped with an Oxford-NordlysNano detector. Post processing of the obtained data was conducted with AZtek 5.0 and HKL Channel 5 software from Oxford Instruments.
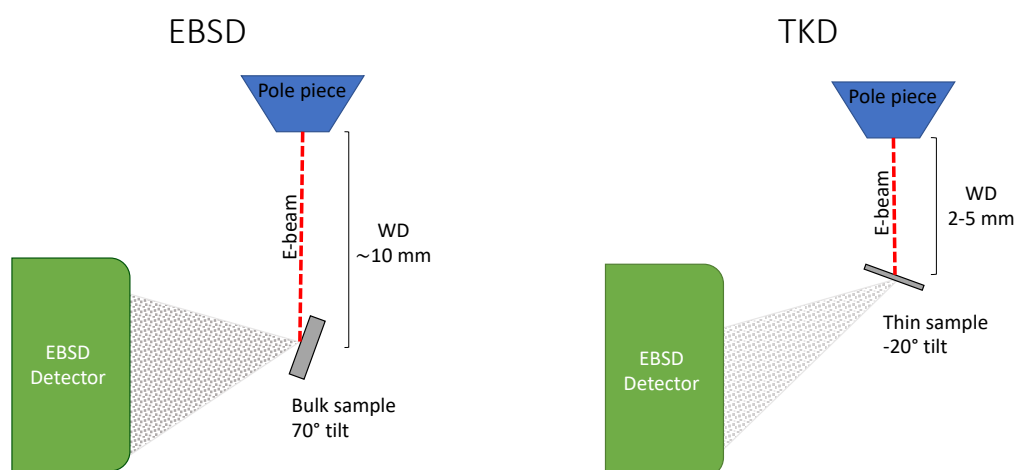

Figure 4-4: Schematic of EBSD sample/detector geometry (left). Schematic of TKD sample/detector geometry (right).

4.2.3 TRANSMISSION ELECTRON MICROSCOPY

Transmission electron microscopy is an extremely powerful microstructural characterization technique. TEM can be used to perform high spatial resolution imaging and to obtain crystallographic and chemical information from the sample. The technique works in transmission which means the specimen needs to be electron transparent, typically a lamella between 20 nm and 200 nm in thickness. TEM can achieve atomic resolution, which makes this technique well suited for all advanced materials characterization needs. The main limitations of this technique lay in the need of a thin sample, which require long and delicate sample preparation, and in the beam sensitivity of some material, that makes it challenging to analyse certain samples without spoiling them. In addition, there are some intrinsic limitations associated with the 2D representation of 3D objects and any TEM based chemical measurement will always have a contribution from the matrix. References for this section are [44,45].

Overview

A schematic of the instrument setup is presented in Figure 4-5. Different TEM instruments can have different setups but a TEM column can generally be divided into three sections: the illuminating system, the image forming system, and the projection and image recording system. In the illuminating system electrons are extracted from the electron gun and subsequently accelerated through the application of high voltage (typically 100 - 300 kV) between the gun and an anode to form the primary e-beam. A first strong condenser lens (C1) collects the emitted electrons from a large solid angle down to a demagnified image of the source. By controlling the strength of C1 and the C1 aperture it is possible to control the electron beam current. One or two additional condenser lenses (C2 and C3) follow C1. C2 project the beam onto the specimen and controls the illumination area. The C2 aperture is used to tune the convergence angle of the beam. With only C2 and C2 aperture it would not be possible to control the illumination area and the convergence angle independently, to solve this, modern instruments have a third set of condenser lens and condenser aperture (C3 and C3 aperture). The image system is made out of objective lenses and the objective aperture. The objective lens determines the final resolution of the instrument and it is responsible for creating both the image of the sample (in the image plane) and the diffraction pattern (in the back focal plane). The specimen is usually inserted between a first and a second part of the objective lens. The selected area diffraction aperture (SAD aperture) is used to select a specific region for electron diffraction. The projection lens magnifies the image or the diffraction pattern onto a fluorescent screen or CCD camera, part of the projection and image recording system. When the instrument has the possibility to work in scanning transmission electron microscopy (STEM) mode, scanning coils will be placed between the illumination system and the image forming system. In this case, an annular dark field (ADF) detector and a high angle annular dark field (HAADF) detector will be present in the image recording system. For elemental analysis, a XEDS detector can be present in close proximity of the specimen and a set of filters, electron prisms and energy selecting slits can be used to perform electron energy loss spectroscopy (EELS) and energy filtered TEM (EFTEM).
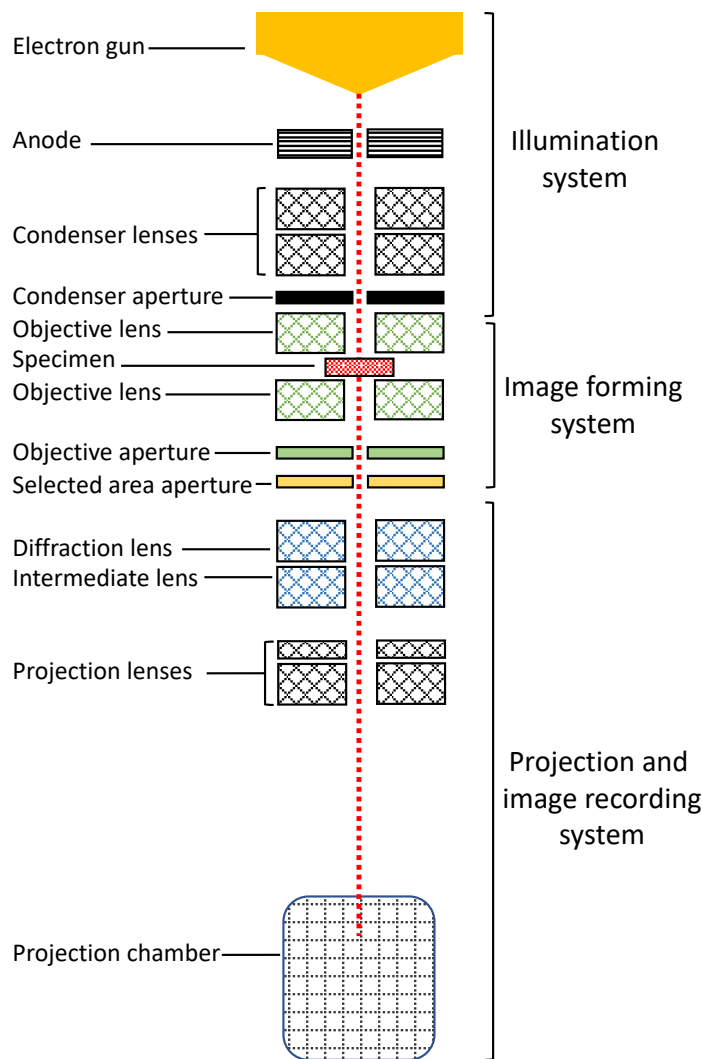
Figure 4-5: Schematic of a TEM column. The illumination system, the image forming system, and the projection and image recording system are roughly shown.

Electron gun — (Illumination system)
Anode —
Condenser lenses —
Condenser aperture —
Objective lens — (Image forming system)
Specimen —
Objective lens —
Objective aperture —
Selected area aperture —
Diffraction lens — (Projection and image recording system)
Intermediate lens —
Projection lenses —
Projection chamber —

TEM mode and STEM mode

In TEM mode the electron beam is parallel and illuminates the specimen uniformly. The electrons move through the specimen and can be un-scattered, elastically scattered or inelastically scattered. Selecting only the un-scattered electrons a bright field (BF) image of the sample is obtained, this imaging mode provides thickness and diffraction contrast. When the elastically scattered electrons are selected to form the image, the result is a dark field (DF) image of the sample. DF imaging provides diffraction contrast. In order to select the un-scattered or elastically scattered electrons, the objective aperture is inserted in the back focal plane and only a specific region of the diffraction pattern is let pass. Conventional TEM imaging can include both signals. Instead, high resolution TEM (HRTEM) imaging is achieved using a large objective aperture (or no objective aperture) and provides phase contrast at atomic resolution. In HRTEM the contrast is produced by the interference of the direct beam and the diffracted beams. The inelastically scattered electrons ca be used for EELS or EFTEM. Characteristic X-rays can be collected with an XEDS detector to obtain chemical information

from the illuminated region of the specimen. In STEM mode the beam is converged into the smallest probe possible for the instrument and this probe is scanned on the sample surface. The signal is collected from each point and integrated in a process conceptually similar to SEM. A smaller probe, and a thin sample, leads to a smaller interaction volume, this significantly increases the XEDS signal resolution. STEM imaging is achieved by collecting the transmitted electrons for each pixels. The BF-STEM collects the un-scattered transmitted electrons and gives mass-thickness contrast and diffraction contrast. ADF imaging collects electrons scattered between 10 and 50 mrad angle, these electrons include Bragg diffracted electrons and inelastically scattered electrons. HAADF imaging is performed collecting the electrons scattered at angles higher than 50 mrad, at this high angles electrons diffracted at the Bragg condition are excluded from the signal and only inelastically scattered electrons remain. Figure 4-6 is used to graphically explain the differences between TEM and STEM modes of operation.
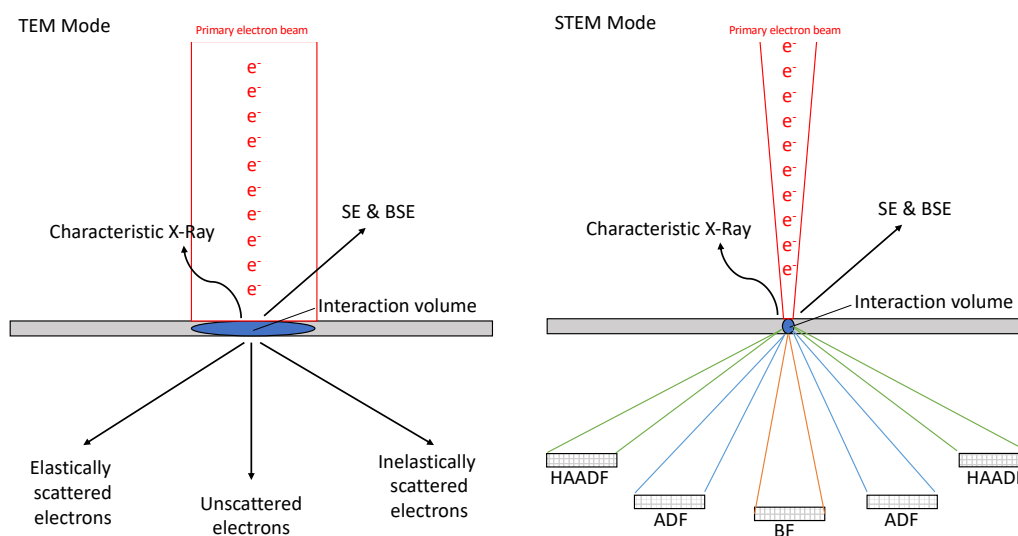

Figure 4-6: Schematic representation of the origin of the different signals used respectively in TEM mode and STEM mode.

An FEI Tecnai T20 equipped with a LaB_6 electron gun was used in this work to collect BF-TEM images of the oxide scale that formed on the CS-Cr coating during autoclave corrosion testing and images of the Cr/Zr interface before and after the exposure. An FEI Titan 80-300 equipped with a FEG electron gun was used to perform HRTEM on the as-fabricated Cr/Zr interface and to study the crystal structure of the material at the interface.

4.2.4   ATOM PROBE TOMOGRAPHY

Overview

Atom probe tomography is one of the techniques that provides the highest resolution for chemical analysis, allowing to study chemical changes down to nearly atomic resolution. It allows to reconstruct the data in 3D making it possible to study small details from all perspectives without having to deal with all artefacts induced by the projection of a 3D object onto a 2D image.

In APT, atoms from needle-shaped specimen are field evaporated in form of ions. These ions are then detected and their mass and position in the sample are identified. The collected data is finally rebuilt into a 3D reconstruction that provides extremely detailed information of the chemical variation in the investigated sample. In order to create the condition for field evaporation to happen, the needle-shaped specimen is kept in an ultra-high vacuum chamber at cryogenic temperatures (30 K − 70 K) while a high positive direct current (DC) voltage is applied between the specimen and an electrode, then a voltage pulse or laser pulse is used to ionize the atoms at the surface of the sample. The ions are then accelerated by the electric field and detected by a 2D position sensitive detector. The time-of-flight for the ions is obtained by measuring how long time passes between the voltage or laser pulse and the detection-event, this time-of-flight allows to extract the mass-to-charge ratio of the ion. Since only the atoms at the very surface of the tip are evaporating, models for the ion trajectory are used to trace backward the ion path to its point of origin. In this way, it possible to reconstruct the specimen, atom by atom, inside a 3D virtual space. A crude schematic illustration of the instrument setup is shown in Figure 4-7. This technique has been historically utilized predominantly for studies of metallic materials, but the development of laser-APT has opened up the possibility to analyse many non-conductive materials. APT is a powerful characterization technique especially for the study of atom clustering in a matrix, solute segregation at grain boundaries or phase interfaces, phase transformations, and nanoscale materials chemistry in general. The main limitations of APT are the small size of the analysed volumes per run, the high mechanical stresses applied on the specimen by the voltage during the analysis, and the significant role of the operator in handling the data reconstruction process. References for this section are [46–48].
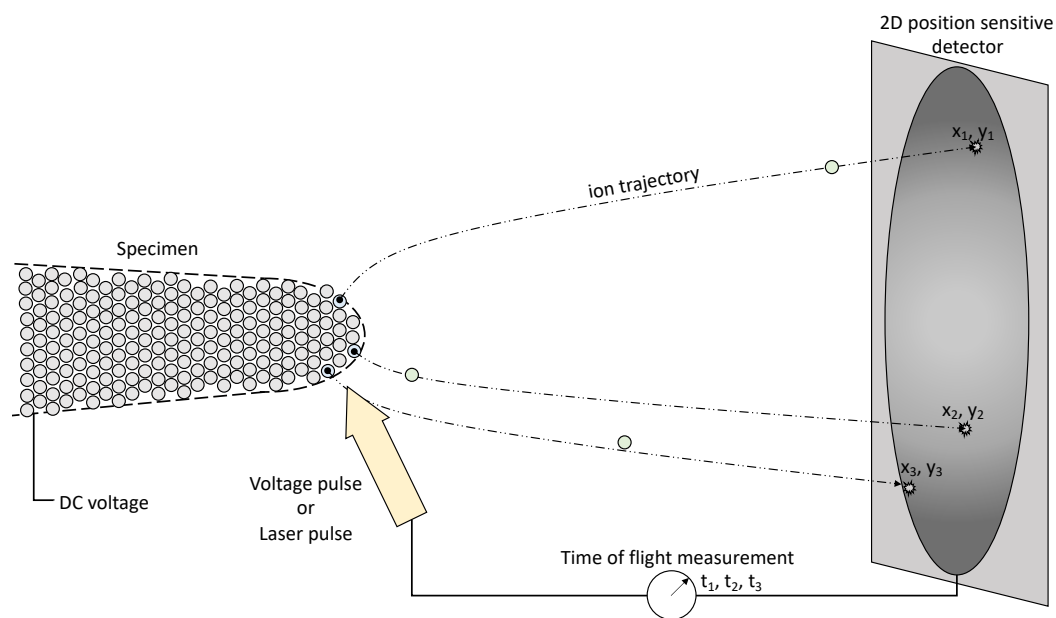

Figure 4-7: Schematic of APT working principle.

Field Evaporation

The field evaporation process is at the core of APT. To bring the specimen atoms close to the evaporation energy barrier a strong DC voltage is applied. The sharp needle-shape of the

specimen further increases the electric field locally experienced by the atoms at the tip of the needle. Assuming the edge of the sample to be a hemisphere with a radius R, a voltage V and field factor k_f, the electric field at the tip of the sample can be calculated using the following equation:

$$ F = \frac{V}{k_f R} \tag{4.1} $$

This field, together with the temperature at which the specimen is kept, determines the coordinates of the atoms onto the field axis and temperature axis of the diagram presented in Figure 4-8. From Equation 4.1 it is clear that the smaller the radius, the higher the field strength will be locally. During the analysis, the specimen will be slowly consumed, the radius R will grow and the DC voltage V will be increased to compensate for this. The penetration depth of the electric field in the sample is extremely shallow (less than a single atomic layer for metals), this ensures that only the atoms at the very surface of the needle will be exposed enough to be close to the evaporation barrier. To push the surface atoms beyond the energy barrier and get them to ionize, extra energy is provided to the system either with a field pulse or a thermal pulse in the form of a DC voltage pulse or a laser pulse, respectively, as shown in Figure 4-8. Field evaporation is a thermally activated process and the most important run parameters that affect this phenomenon are: specimen temperature, voltage or laser pulse frequency, voltage pulse intensity or laser pulse energy, respectively, and evaporation rate (the fraction of the pulses resulting in a detection event).
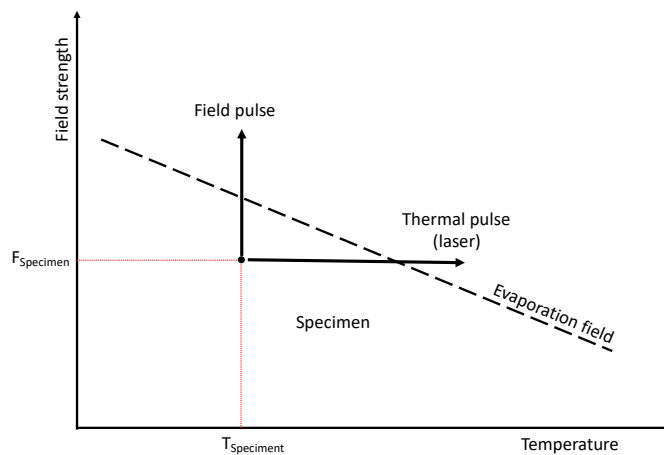

Figure 4-8: Temperature vs Field strength graph, schematic explanation or the role of the voltage/laser pulses.

Data Reconstruction

During the analysis, the x-y position on the detector, the time-of-flight, the voltage applied to the specimen at the time of the event and the other run parameters are saved as data for each single ion. A common analysis can consist of millions of ions and this data needs to be reconstructed before the information about the microchemistry of the sample can be accessed. The atoms that get ionized at the surface of the needle have velocity equal to zero,

they are charged and surrounded by a strong electric field, hence they start accelerating towards the detector. The distance (l) between the specimen and the detector is known and together with the time-of-flight (t_{flight}) it is possible to deduce the mass-to-charge ratio (m/n) of the ion (see Equation 4-2).

$$\frac{m}{n} = 2eV \left(\frac{t_{flight}}{l} \right)^2 \tag{4.2}$$

The mass-to-charge ratio is used for the identification of the ions, an example of a mass spectrum is shown in Figure 4-9. The peaks are then ranged and assigned to a specific element or molecule (in the case of complex ions), this chemical information is then going to be associated with the positional data in order to create the final 3D reconstruction.
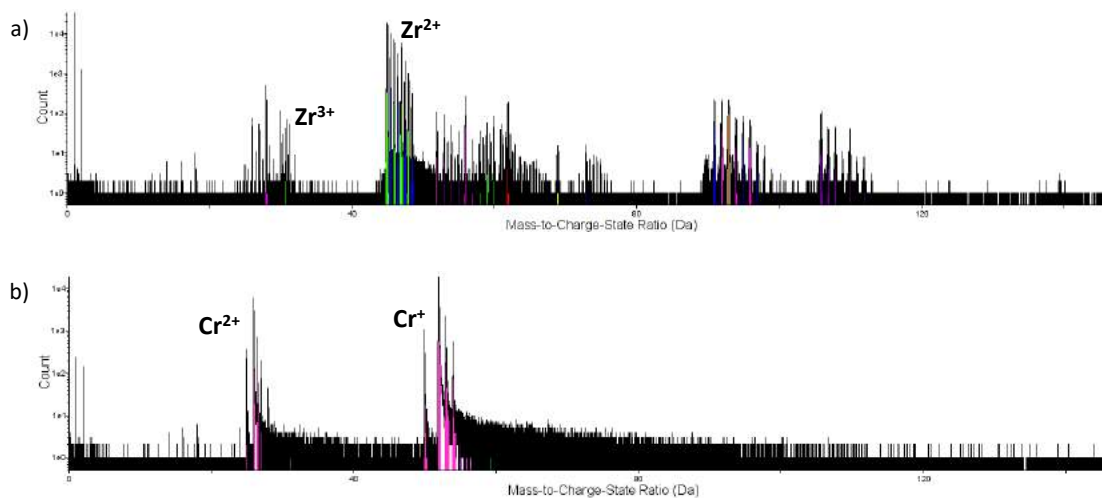

Figure 4-9: Example of mass spectra resulting from analysis of Zr-alloy (a) and pure Cr (b).

The hit coordinates of each ion are used to determine the original position of the atom on the sample surface. The trajectory of the ions is determined by the geometry of the electric field in which they travel and by which they are accelerated. There are different models to determine the ion trajectory and the accuracy of this process can be affected by the material, phases involved in the evaporation process, shape of the tip, etc. Hence, the reconstruction parameters are extremely important for the final geometry of the reconstructed data. Once the final reconstruction is obtained, important information can be extracted using different visualization and quantification tools. One of the most common ways used to display concentration profiles in 3D involves the use of isosurfaces and proxigrams. An isosurface is any surface where the concentration of a selected element (or group of elements) remains constant at a set value. By tuning the selected concentration value, it is possible to identify and isolate microstructural features such as precipitates, grain boundaries or phase boundaries. When the desired isosurface/feature is identified, a proxigram (proximity histogram) can be used to analyse the local atomic neighbourhood adjacent to the isosurface. Each ion is associated with its distance from the isosurface using the normal to the isosurface that pass through the ion position. Using this proxigram algorithm, which is independent of the surface geometry, it is possible to generate histograms displaying the concentration of atoms in a

series of shells increasingly further away from the selected isosurface. What is obtained in practice is the plot of the chemical composition across and away from the isosurface [49,50].

A LEAP 3000X HR Imago Scientific Instruments was used to collect the APT data presented in this work. All samples were run in laser mode with 200 kHz laser pulse frequency, at 50–70 K specimen temperature, 0.3 nJ laser pulse energy and 0.20 % evaporation rate. CAMECA IVAS 3.6.14 software was used for data reconstruction and data evaluation. APT was used to study the chemistry of the Cr/Zr interface in the as-fabricated CS-Cr coated OPZ claddings, to investigate the evolution of the Cr/Zr interface after autoclave exposure and to characterize the oxide formed on the surface of the CS-Cr coating during the autoclave corrosion test.

4.3 SPECIMEN PREPARATION

Specimen Preparation for SEM, EDS and EBSD

Most of the characterization was performed on cladding cross-sections, which provided access to both the Cr/Zr interface and the oxide/coating interface. In addition, a cross-section of the cladding allows to study the substrate microstructure across the entire section which was fundamental in delineating the effects of the CS deposition technique onto the substrate. To prepare the cross-section samples, rings 5 mm in height were cut from the cladding tube with a low-speed saw. The rings were then embedded individually in conductive Bakelite with a mounting press. The obtained samples were ground and polished with SiC-paper and finally with diamond suspensions. This typology of sample was used for SEM investigation and EDS mapping. In order to obtain EBSD quality sample surface, a broad ion beam (BIB) milling system was used. A portion of a ring had to be cut and mounted with the axis perpendicular to the BIB beam. Once mounted, the samples were milled for 10 h at 6 kV beam acceleration voltage, the obtained samples were then analysed directly with EBSD without further surface preparation.

Site Specific Specimen Preparation in FIB/SEM for APT, TEM and TKD

A focused ion beam (FIB) instrument is conceptually similar to an SEM with the important difference of using an ion instead of an electron beam. FIB can be used for imaging but in this work the main application of this technique was as milling tool for *in situ* sample preparation. The FIB/SEM setup used to prepare all the samples analysed with APT and TEM is displayed in Figure 4-10. This instrument is equipped with an electron column mounted vertically and an Ga-ion column mounted at an angle of 52° with respect to the vertical axis (see Figure 4-10 a). A gas injection system (GIS) and a micromanipulator (OmniProbe) are also available and can be used together with the two columns to do in situ work. The SEM is mainly used for imaging, but together with the GIS, the SEM can be also used to deposit metallic Pt on the surface of the sample (electron-deposition). The FIB has imaging capabilities but it is mainly used to deposit metallic Pt together with the GIS or as a milling tool to create wedges, trenches and other structures at the surface of the sample. The OmniProbe is used to extract a small portion of material from the sample to make it possible to prepare TEM lamellas and APT tips. The stage can be tilted at different angles to orient the sample normal towards the electron or the ion beam, respectively, different angles allow to do different type of milling and Pt deposition as shown in Figures 4-10 b and c. In this work, well know procedures for FIB/SEM *in situ* sample preparation were implemented to lift-out portions of material to be analysed in APT and TEM [51–54].
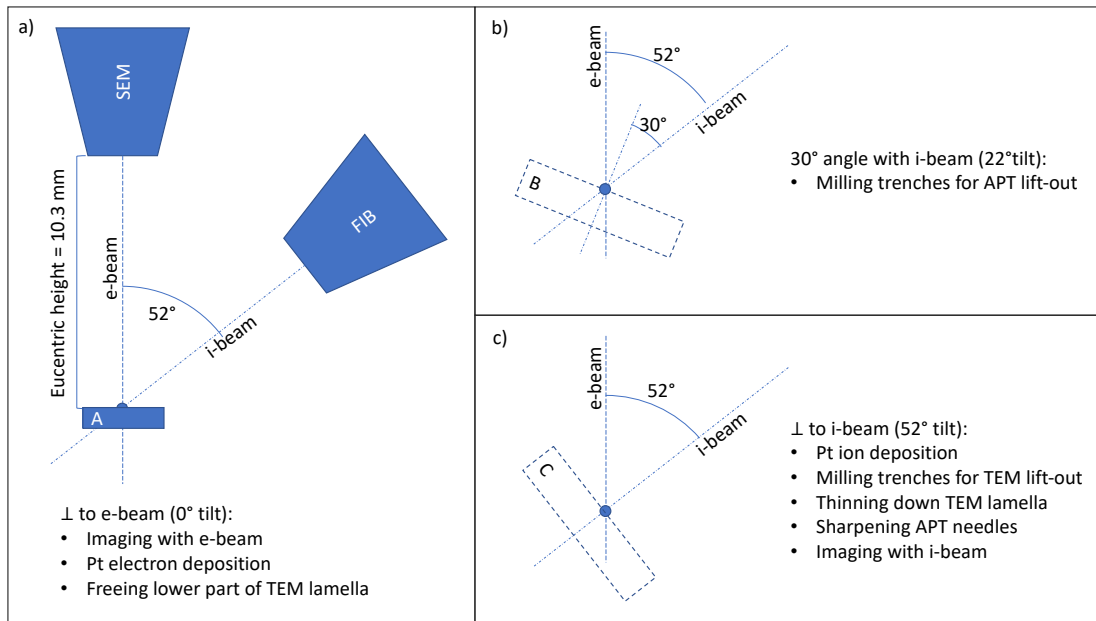
Figure 4-10: Schematic explanation of the FIB/SEM geometry and how the sample is tilted at the different stages of the specimen preparation procedure.

The steps involved in the standard lift-out procedure for APT are presented in Figure 4-11. A thin layer of Pt is deposited on the region of interest with electron-deposition (0° tilt), this step ensures that the desired region is visible and recognisable when using the FIB imaging. The sample is tilted to 52° and additional Pt is deposited with ion-deposition on top of the one obtained with electron-deposition, ion-deposition provides better yields and allows to deposit thicknesses up to one micron. At this point the sample is tilted at 22°, which creates an angle of 30° between the sample surface normal and the ion beam. The FIB is used to mill a trench on one side of the platinum, the sample is rotated 180° and a second trench is milled on the other side of the platinum. The resulting wedge is then set free at one of the two ends. The sample is moved back to 0° tilt, the OmniProbe is inserted inside the analysis chamber and is put into contact with the wedge. Ion-deposition of Pt is used to weld the OmniProbe onto the free end of the wedge, ion milling is used to free the other end of the sample and the volume of interest is extracted from the sample. Once the lift-out is obtained, the far end of the wedge is put in proximity of a pre-made Si-post, it is welded onto the Si-post with some Pt and then the wedge is cut with the FIB to separate the welded portion from the rest of the lift-out (see Figures 4-11 d and e). This last sequence is repeated until the entire lift-out is made into small portions welded onto Si-posts. The final step of sample preparation for APT is the sharpening. At this stage, the sample is tilted to 52° and annular FIB milling is used to reduce the size of the sample down to a sharp needle, as can be seen in Figure 4-11 f (i-v).
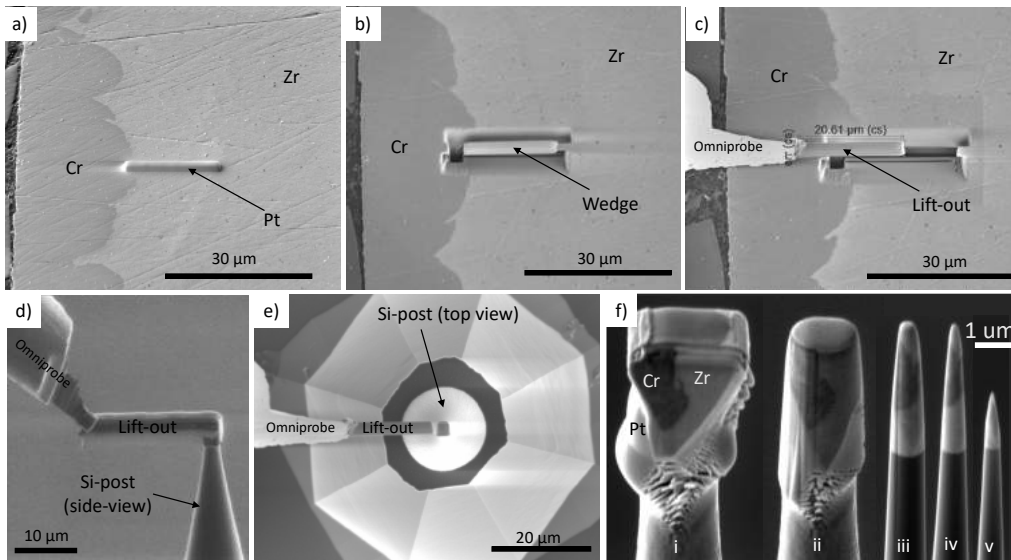
Figure 4-11: In situ lift out procedure for APT: example of steps involved ((a) to (e)). Sharpening of a tip for APT ((f) from i to v).

The procedure for TEM sample preparation has many similarities with the one adopted for APT and it is displayed in Figure 4-12. The region of interest is marked with Pt. The sample is tilted to 52° and this time the milling is done perpendicularly to the surface normal in order to create a lift-out with parallel faces in the shape of a thick lamella. The sample is then tilted to a small angle (between 0° and 7°) and the lift-out is set free with a undercut that leaves only a small portion of material joining the lift-out to the bulk sample. The sample is tilted back to 0°, the OmniProbe is inserted and welded on the lift-out, the thick lamella is set free from the bulk sample, then extracted and mounted onto a Cu half-grid. At this point the sample is tilted to 52° (plus/minus a few degrees), the lamella is thinned and polished down to a thickness of around 50-200 nm using FIB milling.
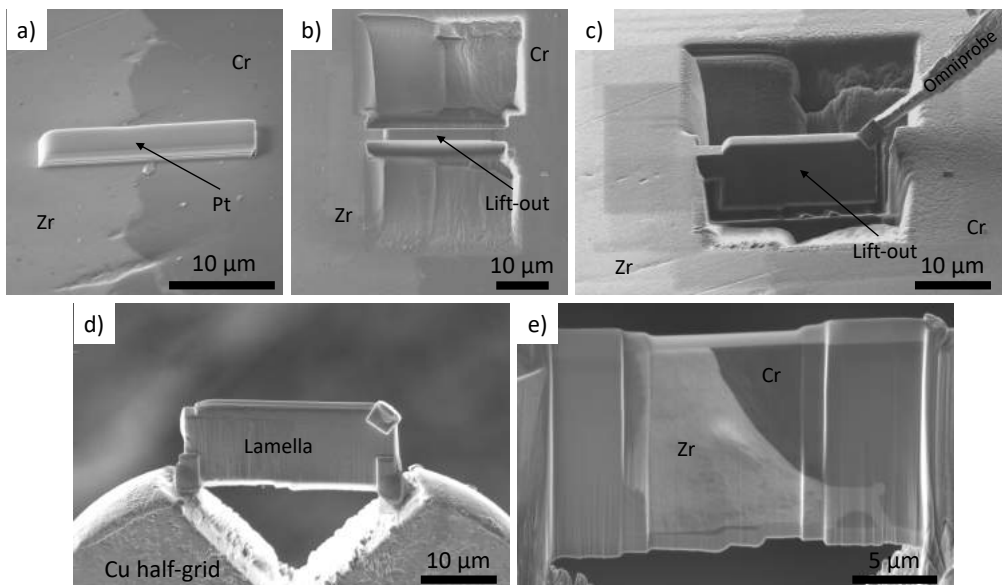

Figure 4-12: In situ lift out procedure for TEM: example of steps involved ((a) to (e)).

SUMMARY OF THE RESULTS

In this section, highlights of the work contained in the appended papers are presented. The experimental results are reorganized with the objective of answering the research questions of this thesis presented in Chapter 1.

5.1 UNDERSTANDING ADHESION IN COLD SPRAY COATINGS

Cold spray coatings have shown great adhesion properties. Shading light on the nature of the strong bond between CS-Cr coatings and the Optimized ZIRLO substrate will help to model the behaviour of this system in operation and under accident conditions. Additionally, it could provide important insights into the phenomena that take place during formation of CS coatings. In Figure 5-1 a, an SEM overview of the coated cladding cross-section is presented. From this image it is possible to appreciate the significant roughness of the Cr/Zr interface. As shown in Figure 5-2 b, both the substrate and the coating particles have suffered heavy plastic deformation. Zr in particular, being the softer of the two metals, has accommodated the Cr particles by wrapping around them and filling all gaps. The result is an interface with a complex shape, where coating and substrate are mechanically interlocked to each other. The convoluted interface represents both a strong advantage and a disadvantage of CS. To the benefits belongs the fact that such a complex geometry makes it difficult for an external load to pull perpendicularly to the interface. This means that even for a weak interfacial bond, the coating would still be stuck, and its spallation would not be easy. The drawback, though, is that such a high degree of roughness reduces inevitably the control over the coating thickness. Although a few micrometres of coating would be sufficient to provide the desired protection, due to the roughness of the interface, more material is needed to cover the entire surface. In those applications where material costs are a limiting factor, this drawback can be significant.

During coating deposition, both the coating particles and the substrate are subjected to deformation that causes fracturing of the native oxide scale, then the gas jet flushes away the oxide debris. The result is an intimate contact between two bare metallic surfaces, as displayed in Figure 5-2 c and Figure 5-2 d. This type of interface is very common for CS coatings and is often referred to as metallurgical bonding. The challenge of studying the metallurgical bonding lays in its very small size (nanometre range). Due to the extremely localized heating and shear deformation that produces the bonding, there is no evidence of diffusion or chemical intermixing in the ranges of magnification that can be explored with techniques as SEM. Even with the conventional TEM imaging, the Cr/Zr interface appears to be a sharp and plain line dividing the coating from the substrate. In order to access this information near atomic resolution is needed and HR-TEM or APT are required.

Figure 5-2 contains the 3D reconstruction of data obtained from an APT analysis of the very interface between Cr and Zr. From this data, a 20 nm thick intermixed bonding region (IBR) emerges and knowledge about the kinetic and thermal history of this region is obtained. From

Figure 5-2 a and Figure 5-2 b it is clear that between a region of pure Cr and a region of pure Zr there is a layer where the Cr and the Zr coexist.
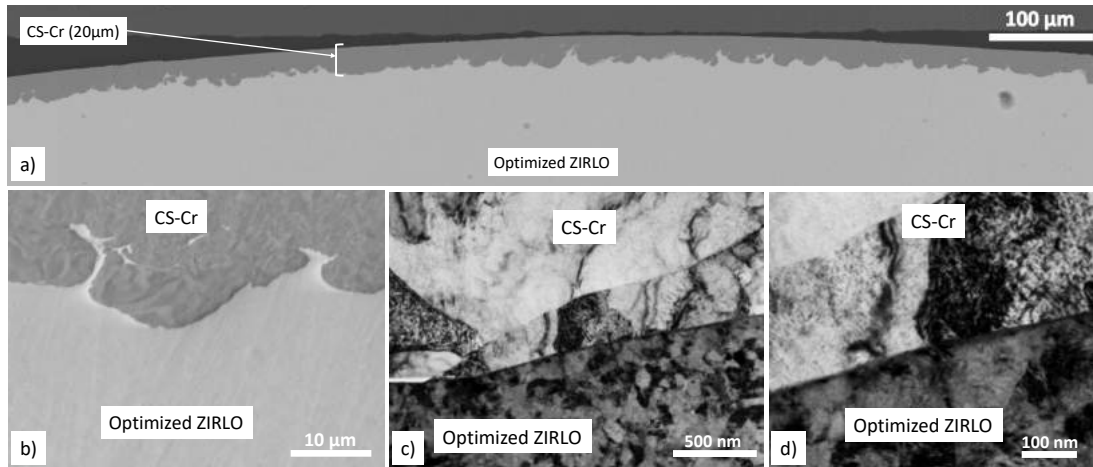

Figure 5-1: Electron microscopy of as-fabricated CS-Cr coated Optimized ZIRLO claddings. (a) and (b) respectively low and high magnification cross-section SEM images. (c) and (d) BF-TEM of Cr/Zr interface.

The average composition of the IBR is approximately 60 at.% Zr, 30 at.% Cr and 10 at.% O as can be extracted from Figure 5-2 d. The Cr/Zr ratio and the presence of oxygen suggest that the zirconium former surface is the main component of the IBR. The layer contains also traces of Sn, Nb, Fe and C (see Figure 5-2 e). Sn, Nb and Fe are alloying elements coming from the Optimized ZIRLO substrate while the carbon could be an impurity potentially originating from grease residues on the former zirconium cladding surface. To have a better view over this layer, a rectangular region of interest is extracted, Figure 5-2 c. Here, two things can be appreciated: the composition of the layer is not uniform and C atoms are mostly concentrated inside Zr-carbide particles. The inhomogeneity of the IBR can be interpreted both as the initial stages of phase separation or as the result of interfacial fluid instabilities. In fact, the composition of the layer falls into a two-phase region where α-Zr and $ZrCr_2$ (Laves phase) are the thermodynamically stable phases. The system, if given the chance, would separate these two phases and the differentiation in Zr-rich regions and Cr-rich regions could be interpreted as the first stage of phase separation. On the other hand, as mentioned in Chapter 3, the highly localized plastic deformation that can affect the particle peripheries and substrate surface, can cause the materials to behave locally like a fluid. When two fluids move at different velocities parallel to their interface, surface instabilities can emerge and develop into whirls at the interface. These whirls could then be quenched in place potentially resulting in the inhomogeneities visible in Figure 5-2 c.
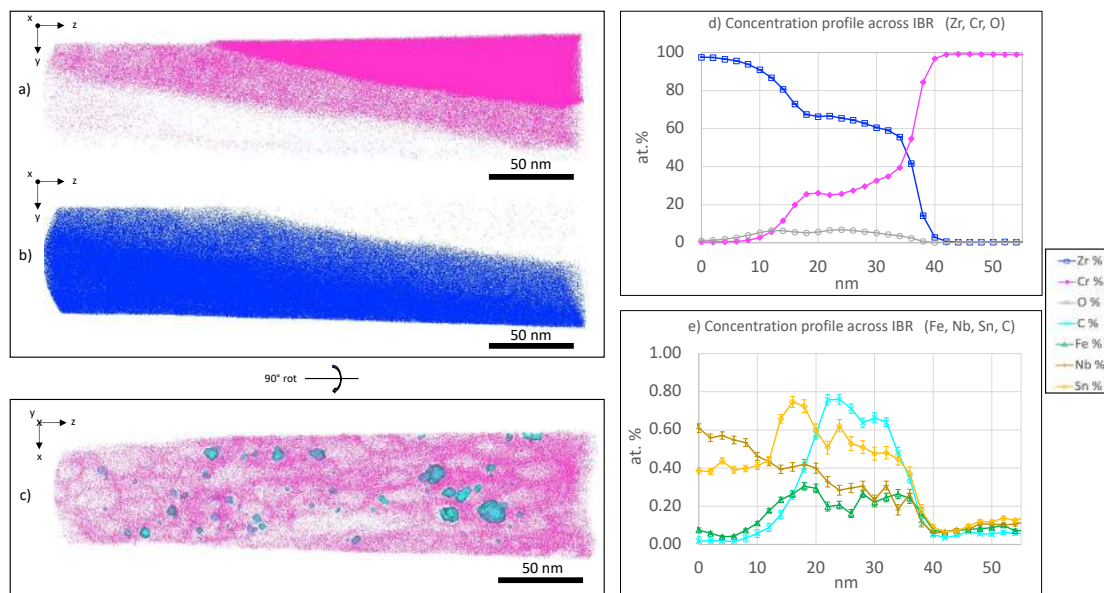
Figure 5-2: 3D reconstruction of APT data from the CS Cr-coating/Optimized ZIRLO™ interface and the area around. In (a) the distribution of Cr atoms (pink, 30% of ions are shown) is displayed, in (b) the distribution of Zr atoms (Blue, 30% of ions are shown) can be seen. (c) An image of a 15 nm slice containing the intermixed bonding region (rotated 90 °) is presented, here the Cr atoms are in pink and the light-blue particles (isosurfaces at 4 at.% C) represent high concentration of C. (d) Concentration profiles across the intermixed bonding region found at the CS Cr-coating/Optimized ZIRLO™ interface.

5.2 High-Strain Deformation Induced Microstructures

The properties of the zirconium cladding tubes are strictly regulated. The main advantage of coated zirconium as ATF solution is that very little modification of the existing material and design is required. Nevertheless, the deposition process can have some effects on the substrate and it is important to verify the entity of such modifications. CS coating formation is based on plastic deformation. The EBSD map presented in Figure 5-3 a, and the TEM images shown in Figure 5-1 c and Figure 5-1 d, allow us to investigate the resulting microstructure of the substrate. The EBSD map shows that the grain structure of the substrate is mostly unaffected by the coating, but some effects start to become visible 10 μm or less form the interface with the coating process. The microstructure of unaffected Optimized ZIRLO claddings is characterized by a mixture of fine, sub-micron grains and larger grains (see bottom region of Figure 5-3 a) while 10 μm from the coating, only the sub-micron grains are visible. Moving even closer to the coating interface, down to a 1-2 μm, the signal from the band contrast map almost disappear. This thin, dark band represents a nanocrystalline layer formed in the Zr-substrate near the interface with the coating. In Figure 5-2 c, the nanocrystalline structure of the Zr can be appreciated more clearly. The size of the Zr grains in the region adjacent to the interface is around 50-100 nm. Interestingly, the grains around the interface appear to be coarser in the Cr than in the Zr. This can probably be explained by the difference in hardness between the two metals and the different degrees of strain the two materials were subjected to as a consequence. The formation of this layer has to be attributed to a dynamic recrystallization phenomenon. At high strains, the large number of dislocations created during

33

plastic deformation start accumulating in dislocation arrays and dislocation walls, evolving eventually in grain boundaries. Through this process, the rotation and tilt introduced into the crystalline lattice by the deformation are accommodated in low energy dislocation structures. With further deformation, these structures can evolve into grain boundaries, finally resulting in fine grains. The same process takes place on the Cr-side, but due to the lower degree of accumulated plastic deformation, the final microstructure of the Cr seems closer to a cell-block structure. In these microstructures, larger regions of material are delimited by thick cell-block boundaries and then further subdivided into cells by thinner dislocation boundaries. The rotation and tilt are usually stored in the cell-block boundaries that work as geometrically necessary boundaries, while the thinner dislocation boundaries emerge mostly as low energy dislocation structures.

The results presented above are a summary of the findings reported in Paper I. The next sections will treat some of the results gathered in Paper II.

5.3 Evolution of the Coating/Substrate System under Operating Conditions

To study the behaviour of the coated cladding and the evolution of the coating/substrate system during operation, the material was exposed to PWR water chemistry in autoclave at 400°-415°C for 90 days. The temperature was chosen to be higher than the normal operation temperature in order to speed up all the thermally activated processes and simulate the equivalent of much longer times at reactor temperature. Given the presence of a nanocrystalline layer at the Cr/Zr interface, if any, thermal recrystallization was expected to occur in such a layer. The microstructure of coating and substrate, before and after autoclave exposure, are compared in Figure 5-3. The first thing that can be noticed is that the Zr-substrate has experienced significant recrystallization, especially further away from the coating. Recrystallization in Optimized ZIRLO is not expected for the operating temperature. The partially recrystallized microstructure typical of this alloy is prone to recrystallization but the threshold temperature for this to happen is usually not reached in operation. The use of a higher temperature for the autoclave testing has activated the recrystallization process, but this result should not be deemed too relevant for the actual performance of the alloy in the reactor. However, this information can be used for comparison with what happens near the interface with the Cr. In the region close to the coating, almost no recrystallization takes place: the nanocrystalline layer seems to have disappeared, but the existing grains are still far below the micron-size range. One possible explanation is that the initial absence of large grains in this region does not create the condition necessary to activate Ostwald ripening. In Ostwald ripening, large grains grow at the expense of smaller grains, but without large grains in the 10 µm region from the coating, there would have been more competition between grains of similar size possibly resulting in less overall recrystallization. Another explanation could be pinning of the grain boundaries by secondary phases. Their presence could slow down grain growth and recrystallization. Assuming the proximity to the coating to be a factor, diffusion of Cr from the coating into the substrate grain boundaries with subsequent nucleation of Cr-rich phases between grains could result in less recrystallization in the region close to the coating. With this scope, APT was used to explore the interfacial region, *Figure 5-4* displays two examples of the main findings. In *Figure 5-4* a, a 50x40 nm particle of $ZrCr_2$ Laves phase is found

at the Cr/Zr interface. The chemical composition of this region is around 60 at.% Cr and 30 at.% Zr, the opposite of the IBR composition measured in the as-fabricated sample. The IBR seems to evolve under autoclave exposure and the system appears to move toward thermodynamic equilibrium phases. The composition and thickness of the IBR after autoclave varies substantially from place to place. Generally, it can be said that there is some degree of chemical evolution happening and that the presence of ZrCr$_2$ nuclei distributed along the interface is the most relevant phenomenon. In fact, the nucleation step of a new phase is the main limiting factor in the precipitation of secondary phases from a solid solution. Hence, if the Laves phase can nucleate already under operating conditions, when given the chance at higher temperature, the ZrCr$_2$ will start growing right away. It is still important to underline that the autoclave temperature was higher than the operating temperature. This difference might have triggered phenomena that would not have happened under normal conditions. Only in-reactor testing over long periods can provide definitive results. The second interesting information provided by the APT investigation is the presence of a Zr-Cr-Fe phase found precipitating at Zr grain boundaries in the substrate adjacent to the Cr/Zr interface in a band a few hundred nanometres thick. The composition of this phase (48 at.% Cr, 44 at.% Zr and 8 at.% Fe), despite small fluctuations, is quite consistent across different regions of the same APT run and across different runs obtained from different regions of the interface. This would suggest that such a phase is nucleating consistently where the right conditions are created. Cr was already found diffusing into the substrate along grain boundaries for similar distances in the as-fabricated material. Hence, it is not too surprising to find it in this phase. Optimized ZIRLO contains small amounts of Fe as alloying element but most of it is usually contained in SPPs. Nevertheless, Fe is a fast diffusor in Zr and it is reasonable to imagine it diffusing and to form energetically favourable phases. The presence of this phase could be one of the factors preventing thermal recrystallization of the substrate region near the interface with Cr.
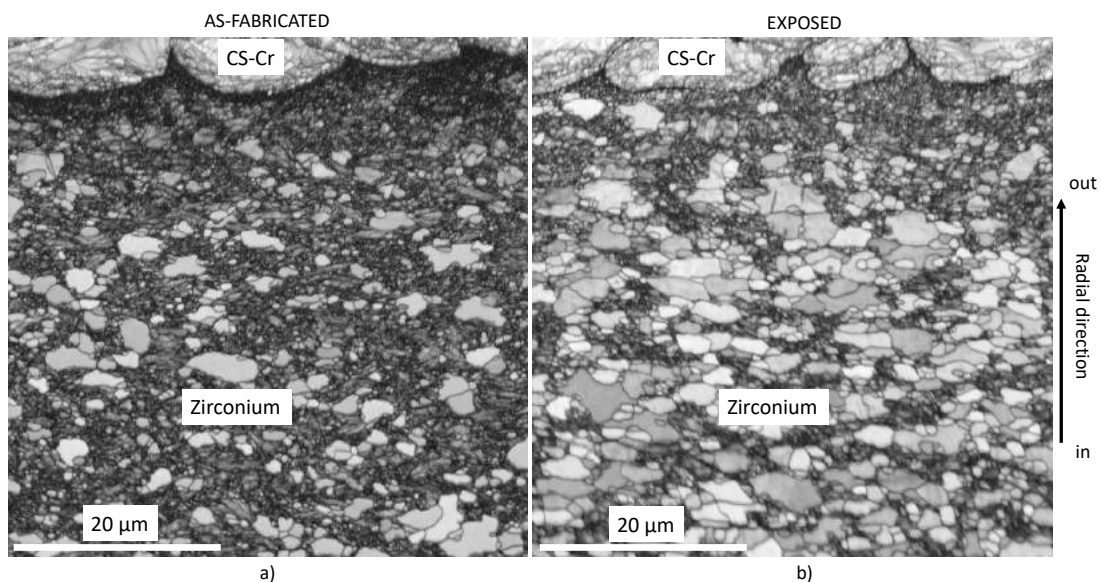

Figure 5-3: EBSD maps over as-fabricated (a) and autoclave exposed (b) CS-Cr coated Optimized ZIRLO cladding cross-sections (Map size 50x50 μm).
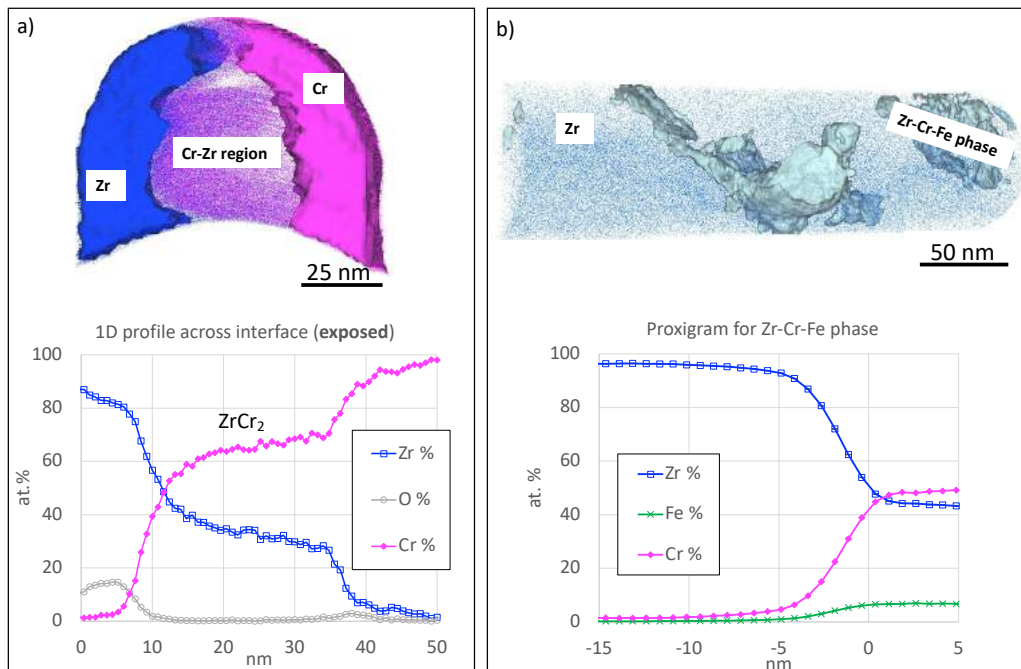
35

Figure 5-4: (a) 3D reconstruction of APT data from the Cr/Zr interface of CS Cr-coated Optimized ZIRLO claddings exposed to autoclave (top). Cr atoms in pink, Zr atoms in blue. The blue surface represents the Zr-substrate, the pink surface represents the Cr-coating. 1D composition profile across Cr/Zr interface of autoclave exposed material (bottom). (b) 3D reconstruction of APT data from the Zr-substrate exposed to autoclave, 100-200 nm distance from the Cr/Zr interface (top). Zr atoms in blue (only 1% shown). Light blue surface encloses a Zr-Cr-Fe phase (isosurface set at Fe+Cr content at 35 at.%). Proxigram across Zr-Cr-Fe phase isosurface (bottom).

5.4 Corrosion Protection under Operating Conditions

The main aim of the ATF concept is to provide better performance than that of traditional materials when exposed to accident conditions. Yet, it is crucial for the accident tolerant material to be able to perform as well, if not better, as the traditional Zr claddings when subject to normal operating conditions. As introduced in Chapter 2, oxidation of Zr cladding is one of the factors limiting fuel rod life and any improvement on this front is considered an additional advantage of the application of the CS-Cr coating. To examine the oxidation protection offered by the Cr coating, cross-sectional TEM imaging and APT were employed (see *Figure 5-5*). From the TEM imaging it is possible to measure the thickness of the oxide scale formed on the surface of the coating during autoclave exposure. This oxide appears to be 50-100 nm thick and compact. The presence of small voids along the oxide/coating interface seems to suggest an outward growth of the oxide. The APT data provides information about the chemical composition of this oxide scale (close to 60 at.% O, 40 at.% Cr) which proves that the oxide is chromia (Cr_2O_3). In the TEM images, small particles can be found further away from the surface of the coating. In APT data these particles appear to be chromia particles. Though, the occurrence of internal oxidation seems unlikely and this oxide particles have probably been embedded in the material during the process of surface grinding and polishing that is performed after the coating deposition. Overall, considering that 1 µm thick oxide can be found on ZIRLO after only 10 days of autoclave exposure at 360°C [55], the development of a 100 nm

thick chromia scale after 90 days at 415°C can be definitively considered a successful improvement.
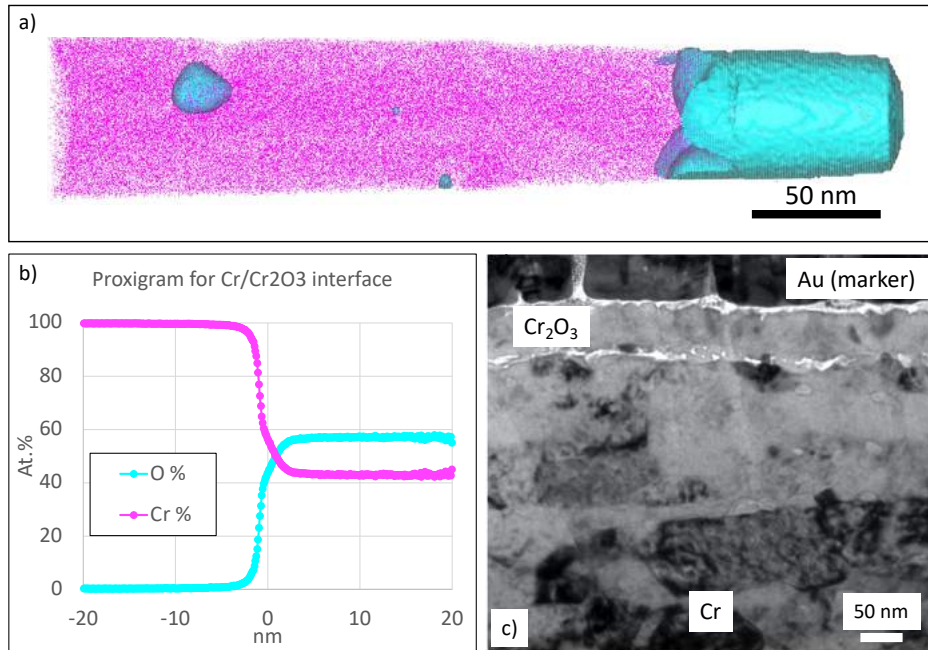

Figure 5-5: (a) 3D reconstruction of APT data from the CS Cr-coating outer surface after autoclave exposure. Cr atoms in pink (30% of ions are shown), the light-blue surfaces represent chromium oxide (isosurfaces at 20 at.% O). (b) Proxigram displaying the composition profile across the Cr/Cr_2O_3 interface. (c) BF-TEM image of Cr_2O_3/Cr interface at the cladding outer surface after autoclave exposure.

5.5 Conclusions

The addition of the CS-Cr coating on top of the Optimized ZIRLO cladding does not affect significantly the substrate microstructure and properties. The formation of a 1-2 µm thick nanocrystalline layer during coating deposition is deemed too thin to modify the mechanical properties of the cladding. Moreover, almost no recrystallization occurs in this region when the material is exposed to normal operating temperatures. The coating's strong adhesion seems to have different origins depending on the scale. At the tens of microns scale, the rough interface produces mechanical interlocking that prevents the very interface from being loaded directly. At the nanometre scale, the presence of a 10-20 nm thick intermixed bonding region is reckoned the origin of the strong metallurgical bond that characterizes CS coatings. Despite small changes in the chemistry and microstructure of the interfacial region taking place during autoclave exposure, neither the nucleation of the Laves phase or (?) the formation of the Zr-Cr-Fe phase can be considered detrimental for the cladding performances under normal operating conditions. The CS-Cr coating seems to provide good oxidation protection. A passivating, 100 nm thick chromia scale forms on the surface of the coated cladding, representing a significant improvement compared to traditional materials. Generally, the coated cladding performs better than the traditional Optimized ZIRLO cladding and the prospect of this ATF concept is very promising.

FUTURE WORK

Development in ATF is progressing fast, many universities and companies are currently working on different solutions ranging from the complete substitution of Zr metal to a variety of coated Zr-claddings. In regard of the coated cladding ATF concept, the main areas where further investigation is needed are:

- Cr-coated Zr-claddings for PWRs
  - In depth study of material exposed to accident conditions (e.g. LOCA tests)
  - In-reactor studies, to study the effect of irradiation

- Coated Zr-claddings for BWRs
  - Identification of a suitable coating (able to withstand BWR environment)
  - Study of material performance under accident conditions
  - In-reactors studies, to study the effect of irradiation

Cr-coated Zr-claddings for PWRs

In the case of PWRs, Cr-coated Zr-claddings perform well and are the main design being considered. The natural steps forward for this material are loss-of-cooling-accident (LOCA) testing and in-reactor testing. The Cr-coating has to withstand accident conditions and has to show that the benefits of it are outweighing the costs and added complexity of manufacturing coated Zr-claddings. Numerous preliminary studies are being performed on samples exposed to high temperature steam oxidation (LOCA simulated environment) and an in-depth characterization of such exposed materials is of crucial importance for the advancement of this design to the commercial stage. Chemical analysis and high-resolution imaging of LOCA tested specimens would provide important input to the understanding and modelling of Cr-coated claddings as accident tolerant materials. For example, following the evolution of the IBR and the growth of the Cr_2O_3-scale after LOCA exposures of different durations would allow to estimate the reaction kinetics and determine for how long the Cr-coating is able to protect the cladding under severe accident conditions. With this scope, SEM, EDS, TEM and APT will be used to probe the chemical changes at different scales. Additionally, to further examine the interaction of Cr-coatings with the core environment, cladding rods need to be tested in running reactors. Many additional elements come into play in a real nuclear reactor, such as irradiation or chemical changes in the water, and no simulated environment can reproduce the entirety of these effects. Though, obtaining and handling such materials is very challenging due to the added complication of the exposure to radiation and rarity of running test reactors.

Coated Zr-claddings for BWRs

When coming to BWRs, the pursuit of a suitable coating is still ongoing. BWRs have a much higher oxygen content in the cooling water than PWRs, which makes it a much more challenging environment for materials to endure. Several coatings, including advanced ceramic coatings, have been tested without any of them emerging as the perfect candidate. Once

identified, the selected material will need to cover all the steps Cr-coatings have been going through. To identify the appropriate candidate, a wide range of coatings will be tested in autoclave and the various samples will be compared to each other and to uncoated zirconium alloy. Once a material that performs well is found, exposed samples will be characterized and compared to the as-fabricated samples in search of interdiffusion between coating and substrate; nucleation, growth and precipitation of new phases; and insight on the oxidation mechanism.

ACKNOWLEDGMENTS

BIBLIOGRAPHY

[1]   W.D. Magwood, H. Paillere, Looking ahead at reactor development, Prog. Nucl. Energy. 102 (2018) 58–67. https://doi.org/10.1016/j.pnucene.2017.07.001.

[2]   International Energy Agency, Nuclear Power in a Clean Energy System, OECD, 2019. https://doi.org/10.1787/fc5f4b7e-en.

[3]   World Nuclear Association, World Nuclear Performance Report 2020, 2020.

[4]   H. Yeom, B. Maier, G. Johnson, T. Dabney, M. Lenling, K. Sridharan, High temperature oxidation and microstructural evolution of cold spray chromium coatings on Zircaloy-4 in steam environments, J. Nucl. Mater. 526 (2019) 151737. https://doi.org/10.1016/j.jnucmat.2019.151737.

[5]   R.B. Rebak, Current materials in light water reactors. Why do we need a materials renewal?, in: Accid. Toler. Mater. Light Water React. Fuels, Elsevier, 2020: pp. 15–41. https://doi.org/10.1016/B978-0-12-817503-3.00002-X.

[6]   K.A. Terrani, Accident tolerant fuel cladding development: Promise, status, and challenges, J. Nucl. Mater. 501 (2018) 13–30. https://doi.org/10.1016/j.jnucmat.2017.12.043.

[7]   M.G. Fontana, R.W. Staehle, Advances in Corrosion Science and Technology, Springer US, Boston, MA, 1972. https://doi.org/10.1007/978-1-4615-8255-7.

[8]   J.P. Foster, H.K. Yueh, R.J. Comstock, M. Limback, B. Kammenzind, S.W. Dean, ZIRLO Cladding Improvement, J. ASTM Int. 5 (2008) 101188. https://doi.org/10.1520/JAI101188.

[9]   IAEA, TECDOC-709: Fuel failure in normal operation of water reactors: experience, mechanisms and management, 1993.

[10]   L.J. Ott, K.R. Robb, D. Wang, Preliminary assessment of accident-tolerant fuels on LWR performance during normal operation and under DB and BDB accident conditions, J. Nucl. Mater. 448 (2014) 520–533. https://doi.org/10.1016/j.jnucmat.2013.09.052.

[11]   R.B. Rebak, Worldwide development of accident tolerant fuels, areas of study, claddings, and fuels, in: Accid. Toler. Mater. Light Water React. Fuels, Elsevier, 2020: pp. 43–62. https://doi.org/10.1016/b978-0-12-817503-3.00003-1.

[12]   R.B. Rebak, Accident-tolerant fuels cladding concept: coatings for zirconium alloys, in: Accid. Toler. Mater. Light Water React. Fuels, Elsevier, 2020: pp. 63–81. https://doi.org/10.1016/b978-0-12-817503-3.00004-3.

[13]   S. Tuzi, K. Göransson, S.M.H. Rahman, S.G. Eriksson, F. Liu, M. Thuvander, K. Stiller, Oxide evolution on Alloy X-750 in simulated BWR environment, J. Nucl. Mater. 482 (2016) 19–27. https://doi.org/10.1016/j.jnucmat.2016.09.026.

[14]   S. Tuzi, H. Lai, K. Göransson, M. Thuvander, K. Stiller, Corrosion of pre-oxidized nickel alloy X-750 in simulated BWR environment, J. Nucl. Mater. 486 (2017) 350–360.

https://doi.org/10.1016/j.jnucmat.2017.01.051.

[15]   L. Tan, T. Chen, B.A. Pint, Steam oxidation behavior of Ni-base superalloys 690, 725 and X-750 at 600 and 650 °C, Corros. Sci. 157 (2019) 487–497. https://doi.org/10.1016/j.corsci.2019.06.014.

[16]   J.C. Brachet, M. Le Saux, M. Le Flem, S. Urvoy, E. Rouesne, T. Guilbert, C. Cobac, F. Lahogue, J. Rousselot, M. Tupin, P. Billaud, C. Hossepied, F. Schuster, F. Lomello, A. Billard, G. Velisa, E. Monsifrot, J. Bischoff, A. Ambard, On-going studies at CEA on chromium coated zirconium based nuclear fuel claddings for enhanced Accident Tolerant LWRs Fuel, in: TopFuel, 2015: pp. 31–38.

[17]   J. Bischoff, C. Delafoy, C. Vauglin, P. Barberis, C. Roubeyrie, D. Perche, D. Duthoo, F. Schuster, J.C. Brachet, E.W. Schweitzer, K. Nimishakavi, AREVA NP's enhanced accident-tolerant fuel developments: Focus on Cr-coated M5 cladding, Nucl. Eng. Technol. 50 (2018) 223–228. https://doi.org/10.1016/j.net.2017.12.004.

[18]   B. Maier, H. Yeom, G. Johnson, T. Dabney, J. Walters, P. Xu, J. Romero, H. Shah, K. Sridharan, Development of cold spray chromium coatings for improved accident tolerant zirconium-alloy cladding, J. Nucl. Mater. 519 (2019) 247–254. https://doi.org/10.1016/j.jnucmat.2019.03.039.

[19]   J. Bischoff, C. Delafoy, N. Chaari, C. Vauglin, K. Buchanan, P. Barberis, E. Monsifrot, J.-C.B. F. Schuster, K. Nimishakavi, Cr coated cladding Development At Framatome, in: TopFuel, 2018: pp. 1–7.

[20]   B. Maier, H. Yeom, G. Johnson, T. Dabney, J. Walters, J. Romero, H. Shah, P. Xu, K. Sridharan, Development of Cold Spray Coatings for Accident-Tolerant Fuel Cladding in Light Water Reactors, JOM. 70 (2018) 198–202. https://doi.org/10.1007/s11837-017-2643-9.

[21]   H. Yeom, B.R. Maier, G. Johnson, K. Sridharan, Cold Spray Coatings for Accident Tolerant Zr-Alloy Cladding in Light Water Reactors, in: Trans. Am. Nucl. Soc., 2018: pp. 1576–1579. https://www.researchgate.net/publication/325812110 (accessed December 19, 2018).

[22]   R. V. Umretiya, B. Elward, D. Lee, M. Anderson, R.B. Rebak, J. V. Rojas, Mechanical and chemical properties of PVD and cold spray Cr-coatings on Zircaloy-4, J. Nucl. Mater. 541 (2020) 152420. https://doi.org/10.1016/j.jnucmat.2020.152420.

[23]   J.C. Brachet, E. Rouesne, J. Ribis, T. Guilbert, S. Urvoy, G. Nony, C. Toffolon-Masclet, M. Le Saux, N. Chaabane, H. Palancher, A. David, J. Bischoff, J. Augereau, E. Pouillier, High temperature steam oxidation of chromium-coated zirconium-based alloys: Kinetics and process, Corros. Sci. 167 (2020) 108537. https://doi.org/10.1016/j.corsci.2020.108537.

[24]   J. Hazan, A. Gauthier, E. Pouillier, K. Shirvan, Semi-integral LOCA test of cold-spray chromium coated zircaloy-4 accident tolerant fuel cladding, J. Nucl. Mater. 550 (2021) 152940. https://doi.org/10.1016/j.jnucmat.2021.152940.

[25]   A.P. Alkhimov, A.N. Papyrin, U. Vyazemskogo, V.F. Kosarev, N.I. Nesterovich, M.M. Shushpanov, United States Patent - Gas-dynamic spraying method for applying a

coating, 1994. https://patents.google.com/patent/US5302414A/en (accessed April 22, 2021).

[26]   V.K. Champagne, The cold spray materials deposition process, Woodhead Publishing Limited, 2007. https://doi.org/10.1533/9781845693787.

[27]   P. Cavaliere, Cold-Spray Coatings: Recent Trends and Future perspectives, Springer, 2017. https://doi.org/10.1007/978-3-319-67183-3.

[28]   Y. Xu, I.M. Hutchings, Cold spray deposition of thermoplastic powder, Surf. Coatings Technol. 201 (2006) 3044–3050. https://doi.org/10.1016/j.surfcoat.2006.06.016.

[29]   Y. Ichikawa, R. Tokoro, M. Tanno, K. Ogawa, Elucidation of cold-spray deposition mechanism by auger electron spectroscopic evaluation of bonding interface oxide film, Acta Mater. 164 (2019) 39–49. https://doi.org/10.1016/j.actamat.2018.09.041.

[30]   X.T. Luo, Y. Ge, Y. Xie, Y. Wei, R. Huang, N. Ma, C.S. Ramachandran, C.J. Li, Dynamic evolution of oxide scale on the surfaces of feed stock particles from cracking and segmenting to peel-off while cold spraying copper powder having a high oxygen content, J. Mater. Sci. Technol. 67 (2021) 105–115. https://doi.org/10.1016/j.jmst.2020.06.019.

[31]   J. Karthikeyan, The advantages and disadvantages of the cold spray coating process, in: Cold Spray Mater. Depos. Process, Woodhead Publishing Limited, 2007: pp. 62–71. https://doi.org/10.1201/9781439824122.ch4.

[32]   X.J. Ning, J.H. Jang, H.J. Kim, The effects of powder properties on in-flight particle velocity and deposition process during low pressure cold spray process, Appl. Surf. Sci. 253 (2007) 7449–7455. https://doi.org/10.1016/j.apsusc.2007.03.031.

[33]   F.J. Brodmann, Cold spray process parameters: Powders, in: V.K.B.T.-T.C.S.M.D.P. Champagne (Ed.), Cold Spray Mater. Depos. Process Fundam. Appl., Woodhead Publishing, 2007: pp. 105–116. https://doi.org/10.1533/9781845693787.2.105.

[34]   H. Yeom, T. Dabney, G. Johnson, B. Maier, M. Lenling, K. Sridharan, Improving deposition efficiency in cold spraying chromium coatings by powder annealing, Int. J. Adv. Manuf. Technol. 100 (2019) 1373–1382. https://doi.org/10.1007/s00170-018-2784-1.

[35]   M. Grujicic, Particle/substrate interaction in the cold-spray bonding process, in: Cold Spray Mater. Depos. Process, Woodhead Publishing Limited, 2007: pp. 148–177. https://doi.org/10.1201/9781439824122.ch9.

[36]   O. Bielousova, J. Kocimski, R.G. Maev, I. Smurov, W. Scharff, V. Leshchynsky, Localisation of deformation in cold gas dynamic spraying, Surf. Eng. 32 (2016) 655–662. https://doi.org/10.1179/1743294415Y.0000000059.

[37]   H. Assadi, F. Gärtner, T. Stoltenhoff, H. Kreye, Bonding mechanism in cold gas spraying, Acta Mater. 51 (2003) 4379–4394. https://doi.org/10.1016/S1359-6454(03)00274-X.

[38]   C. Lee, J. Kim, Microstructure of Kinetic Spray Coatings: A Review, J. Therm. Spray

Technol. 24 (2015) 592–610. https://doi.org/10.1007/s11666-015-0223-5.

[39] M. Grujicic, C.L. Zhao, W.S. DeRosset, D. Helfritch, Adiabatic shear instability based mechanism for particles/substrate bonding in the cold-gas dynamic-spray process, Mater. Des. 25 (2004) 681–688. https://doi.org/10.1016/j.matdes.2004.03.008.

[40] W. Conshohocken, ASTM G2/G2M - 19: Standard Test Method for Corrosion Testing of Products of Zirconium, Hafnium, and Their Alloys in Water at 680°F (360°C) or in Steam at 750°F (400°C), 88 (1996) 1–8. https://doi.org/10.1520/G0002-88R02.

[41] J.I. Goldstein, D.E. Newbury, J.R. Michael, N.W.M. Ritchie, J.H.J. Scott, D.C. Joy, Scanning electron microscopy and x-ray microanalysis, Springer, 2017. https://doi.org/10.1007/978-1-4939-6676-9.

[42] W. Zhou, Z.L. Wang, Scanning microscopy for nanotechnology: Techniques and applications, Springer New York, New York, NY, 2007. https://doi.org/10.1007/978-0-387-39620-0.

[43] A.J. Schwartz, M. Kumar, B.L. Adams, eds., Electron Backscatter Diffraction in Materials Science, Springer US, Boston, MA, 2000. https://doi.org/10.1007/978-1-4757-3205-4.

[44] D.B. Williams, C.B. Carter, Transmission electron microscopy: A textbook for materials science, 2009. https://doi.org/10.1007/978-0-387-76501-3.

[45] C.B. Carter, D.B. Williams, Transmission electron microscopy: Diffraction, imaging, and spectrometry, Springer US, Boston, MA, 2016. https://doi.org/10.1007/978-3-319-26651-0.

[46] M.K. Miller, R.G. Forbes, Atom-probe tomography: The local electrode atom probe, Springer US, Boston, MA, 2014. https://doi.org/10.1007/978-1-4899-7430-3.

[47] M.K. Miller, Atom Probe Tomography, Springer US, Boston, MA, 2000. https://doi.org/10.1007/978-1-4615-4281-0.

[48] B. Gault, M.P. Moody, J.M. Cairney, S.P. Ringer, Atom Probe Microscopy, Springer New York, New York, NY, 2012. https://doi.org/10.1007/978-1-4614-3436-8.

[49] O.C. Hellman, D.N. Seidman, Measurement of the Gibbsian interfacial excess of solute at an interface of arbitrary geometry using three-dimensional atom probe microscopy, Mater. Sci. Eng. A. 327 (2002) 24–28. https://doi.org/10.1016/S0921-5093(01)01885-8.

[50] B. Gault, M.P. Moody, J.M. Cairney, S.P. Ringer, Atom Probe Microscopy and Materials Science, in: Springer New York, New York, NY, 2012: pp. 299–311. https://doi.org/10.1007/978-1-4614-3436-8_9.

[51] R.M. Langford, M. Rogers, In situ lift-out: Steps to improve yield and a comparison with other FIB TEM sample preparation techniques, Micron. 39 (2008) 1325–1330. https://doi.org/10.1016/j.micron.2008.02.006.

[52] K. Thompson, D. Lawrence, D.J. Larson, J.D. Olson, T.F. Kelly, B. Gorman, In situ site-

specific specimen preparation for atom probe tomography, Ultramicroscopy. 107 (2007) 131–139. https://doi.org/10.1016/j.ultramic.2006.06.008.

[53]   L.A. Giannuzzi, F.A. Stevie, Introduction to focused ion beams: Instrumentation, theory, techniques and practice, Springer, 2005. https://doi.org/10.1007/b101190.

[54]   D. Tomus, H.P. Ng, In situ lift-out dedicated techniques using FIB-SEM system for TEM specimen preparation, Micron. 44 (2013) 115–119. https://doi.org/10.1016/j.micron.2012.05.006.

[55]   J. Wei, P. Frankel, E. Polatidis, M. Blat, A. Ambard, R.J. Comstock, L. Hallstadius, D. Hudson, G.D.W. Smith, C.R.M. Grovenor, M. Klaus, R.A. Cottis, S. Lyon, M. Preuss, The effect of Sn on autoclave corrosion performance and corrosion mechanisms in Zr-Sn-Nb alloys, Acta Mater. 61 (2013) 4200–4214. https://doi.org/10.1016/j.actamat.2013.03.046.